https://doi.org/10.1038/s44335-025-00034-4

Two-dimensional material-based devices for in-sensor computing

Jinli Chen[1], Weigang Wang[2] & Xiaodong Yan[1,3,4] ✉

In-sensor computing (ISC) integrates sensing, memory, and processing at the point of data acquisition, enabling real-time, low-power operation. Two-dimensional (2D) materials offer unique advantages for ISC due to their atomic thickness and multifunctional properties. This review highlights 2D material-based ISC devices, covering mechanisms, performance, and architectures, and discusses challenges and solutions toward scalable fabrication and practical deployment in emerging technologies like Internet of Things (IoT), analog computing, and motion detection.

Background and motivation for 2D in-sensor computing

Due to the explosive growth of the IoT[1,2] and artificial intelligence (AI)[3,4], novel computing schemes capable of efficiently handling massive data are crucially needed[5,6]. By 2025, a total of 80 zettabytes of data will be collected and processed by global IoT devices[7]. Traditional computing schemes relying on von Neumann architectures, which separate memory, sensing and computing hardware, result in frequent data transfer with undesirable latency and power consumption[8,9]. ISC is an emerging solution to the von Neumann bottleneck, incorporating both processing and memory within sensors to facilitate real-time decision-making with low power consumption[5,10–12] (Fig. 1).

2D material-based ISC devices distinguish themselves from other ISC technologies by offering unparalleled properties such as high sensing sensitivity[13], high-density memory states[14], and good compatibility with materials in various dimensions[15–17]. 2D materials enable efficient sensing of light, temperature, magnetic fields and mechanical stress with strong optoelectronic responses[18], rapid temperature-dependent phase transitions[19], intrinsic spin alignment[20], and strong piezoelectric effects[21]. 2D material-based memory devices exhibit up to 1280 memory states[14], leading to high-resolution information storage. Mixed-dimensional integrating 2D materials onto complementary metal-oxide-semiconductor (CMOS) circuits[15] or flexible substrates[22,23] lead to the discovery of 2D devices with unprecedent functionality and enhanced wearability. 2D ISC devices offer strong potential in biomedical fields where real-time, on-device processing of multiple input signals is critical[24], including brain-machine interfaces[25,26], seizure detection systems[27,28], and health monitoring platforms[29,30]. With more 2D material properties being unveiled, the ISC capabilities of 2D material-based devices continue to evolve rapidly[31].

Many 2D ISC applications such as adaptive behavior[32,33], associative learning[33–35], pattern recognition[36,37], and edge detection[38,39] have been demonstrated. These applications are realized through three distinct ways: using single multifunctional device[35], deploying arrays of ISC devices[38,40], and heterogeneously integrating sensing and memory devices[41]. A multifunctional single device, which integrates sensing and computation within a single 2D platform, offers a compact and cost-effective approach to ISC. Scaling individual devices into array-based ISC configuration enhances parallel processing speed and sensing resolution. It requires complex fabrication techniques to minimize device-to-device variation[19]. Alternatively, hybrid integration systems, combining top-tier sensors and memory devices of cross-species in a modular manner[42], merge their complementary strengths for enhanced functionality. It requires optimized coupling and interconnection strategies to maximize efficiency[41].

This review begins by exploring state-of-the-art 2D material-based ISC devices. In Sections "Ferroelectric devices" and "Memristor and Memristive devices", we discuss ferroelectric (FE) and memristive devices, analyzing their operational mechanisms, performance metrics, and ISC applications. We then explore the potential of utilizing the unique spatially modulated electronic phases in 2D materials for next-generation ISC devices. Section "Charge density wave devices" delves into charge-density-wave-based devices, while Section "Spintronic devices" examines spin-based devices. These devices hold promise for ISC due to their ultrafast switching dynamics and high sensitivity to optical and magnetic stimuli. Key challenges and future directions in 2D devices-based ISC research are elaborated in Section "Summary and Outlook", where we discuss the strategies for advancing real-time multimodal ISC applications, the development of emerging 2D topological insulators with unique sensing capabilities, and approaches toward wafer-scale integrations.

Ferroelectric devices

Ferroelectricity originates from non-centrosymmetric crystal structures, where polarization emerges via subtle ionic displacements[43,44]. This

[1]Department of Materials Science and Engineering, University of Arizona, Tucson, AZ, USA. [2]Department of Physics, University of Arizona, Tucson, AZ, USA. [3]Department of Electrical and Computer Engineering, University of Arizona, Tucson, AZ, USA. [4]James C. Wyant College of Optical Sciences, University of Arizona, Tucson, AZ, USA. ✉e-mail: xyan@arizona.edu

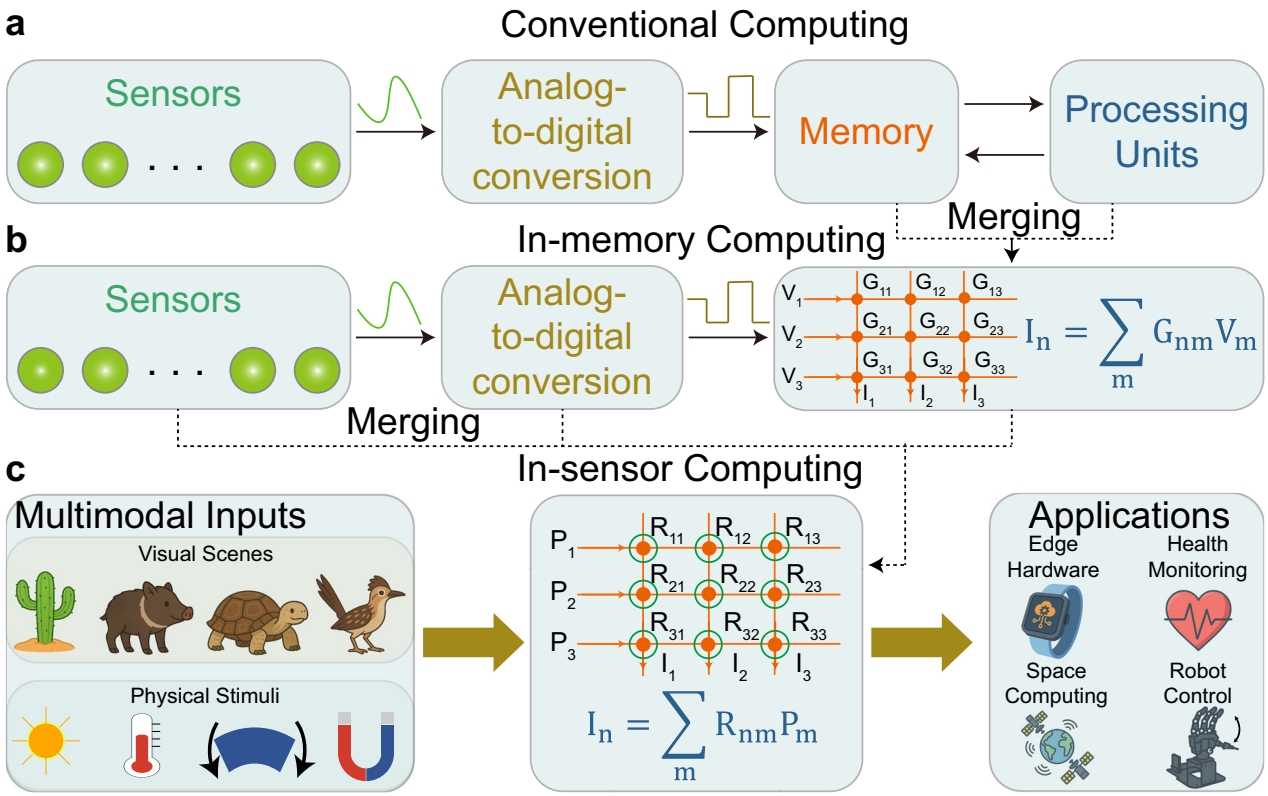

Fig. 1 | Conceptual illustration of in-sensor computing. a In conventional computing, sensors, memory, and processing are physically separated. Signals from sensors undergo analog-to-digital conversion before being processed. **b** In in-memory computing, data processing occurs directly within memory arrays, but sensors remain separate. **c** In in-sensor computing, sensors, memory, and computing are physically integrated into a single platform. The bottom-left panel illustrates multimodal inputs, including visual scenes (e.g., cactus, javelina, tortoise, and roadrunner) and physical stimuli (e.g., light, temperature, strain, and magnetic fields). These inputs are encoded and processed in a distributed resistive network, leading to applications such as edge hardware, space computing, health monitoring, and robot control.

polarization can be reversibly switched by electric fields, allowing for non-volatile data storage, erasure, and reprogramming[45]. Depending on the origin of ferroelectricity, 2D FE devices are categorized into three types: intrinsic FE devices, interfacial FE devices, and interlayer FE devices. Intrinsic FE devices utilize 2D materials with inherent FE properties, such as In_2Se_3[46], SnS[47], SnSe[48] and $CuInP_2S_6$ (CIPS)[49], as the active channels or gate dielectrics (Fig. 2a). Interfacial FE devices employ non-ferroelectric 2D materials (e.g., MoS_2, WSe_2) as channels, paired with traditional 3D FE materials (e.g., barium titanate (BTO)[50] and poly(vinylidenefluoride-trifluoroethylene) P(VDF-TrFE)[38]) as gate-dielectric to modulate charge transport (Fig. 2b). Interlayer FE devices exploit the non-centrosymmetric polarization induced by sliding[51] or rotating[52] between 2D materials (Fig. 2c, d).

Two widely studied intrinsic FE materials for 2D ISC devices are α-In_2Se_3 and CIPS. The α-In_2Se_3 exhibits two distinct ground polar states driven by the motion of the middle Se atom, resulting in interlocked in-plane (IP) and OOP polarizations[43]. This interlocking effect stabilizes ferroelectricity even at the monolayer limit[53]. The FE polarization in α-In_2Se_3 can be further controlled by illumination in a non-destructive manner, leading to applications including photon detectors and optoelectrical memory[54]. These properties positions α-In_2Se_3 as a workforce material for 2D FE ISC devices (Fig. 2e)[35,55–57]. For example, α-In_2Se_3/SnSe based p-n junctions emulate synaptic behaviors, including short-term/long-term plasticity (STP/LTP) and excitatory/inhibitory functions, achieving a ultra-high paired-pulse facilitation (PPF) index of 457% which is crucial for promoting the development of artificial vision[35] (Fig. 2f). The p-n junctions implement Pavlovian associative learning: an initial conditioned stimulus (CS, +2 V electrical pulse) induces a subthreshold current (0.12 nA < I_{th} = 0.14 nA), failing to trigger a response. After five co-stimulation cycles with an unconditioned stimulus (US, 0.69 mW cm^{-2} light), the current surges to ≈1.68 nA, establishing a strong associative reflex. Subsequent CS stimuli alone generate suprathreshold currents (0.16 nA), confirming the circuit's ability to retain and execute the learned CS-US association.

CIPS exhibits spontaneous OOP polarization due to the displacement of Cu atoms from their lattice centers and the cation displacement in the In lattice[49,58]. Its insulating nature (bandgap ~ 2.9 eV), high tunneling electroresistance[59], and dangling-bond-free surface[60] support robust non-volatile FE memory functionality. While recent studies demonstrate light-induced polarization switching in CIPS[61,62], its role in ISC remains limited to gate modulation rather than direct light-sensing channels. For instance, SnS_2/hexagonal boron nitride (h-BN)/CIPS-based ferroelectric field-effect transistors (Fe-FETs) utilize the optoelectrical properties of SnS_2 and the ferroelectricity of CIPS to emulate optoelectrical synaptic behaviors[34]. These Fe-FETs form a fully FET-driven reservoir computing (RC) system with a reservoir layer and a fully connected layer. In the reservoir layer, Fe-FETs with optical STP process stimulus-dependent current relaxation. In the fully connected layer, Fe-FETs with electrical LTP and long-term depression serve as tunable synaptic weights for training and classification. This RC system achieves 93.62% accuracy in MNIST image recognition, showcasing a streamlined approach to ISC. CIPS can integrate with telecom-wavelength materials, as shown in CIPS/graphene/h-BN/Te FE-FETs[37], where the thickness-tunable bandgap of Te enables efficient 1550 nm (telecom-band) photoresponse. When integrated into an RC system, these Fe-FETs directly process optical fiber signals, achieving ~80% accuracy in digit recognition.

2D Janus MoSSe exhibits spontaneous OOP polarization due to its asymmetric structure, which breaks the OOP structural symmetry of MoS_2[63].

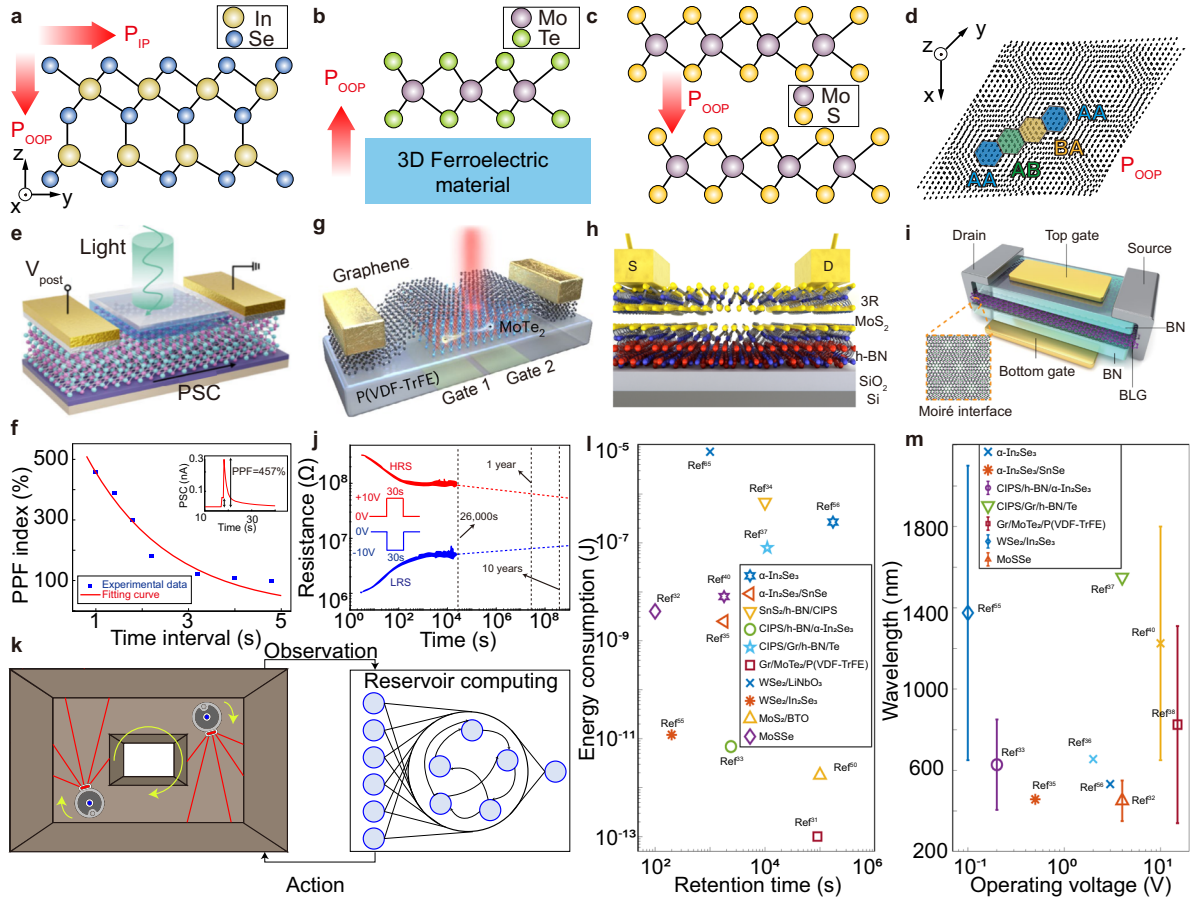

Fig. 2 | 2D FE devices for in-sensor computing. a Schematic of intrinsic ferroelectricity in In_2Se_3, where the displacement of the central Se atom induces interlocked in-plane and out-of-plane polarizations. **b** Schematic of interfacial ferroelectricity, where 3D ferroelectric materials modulate charge carrier concentration in 2D materials, leading to resistance changes. **c** OOP sliding ferroelectricity in bilayer MoS_2 due to charge center displacement. **d** Schematic of excitonic ferroelectricity arising from asymmetric moiré structure. **e** The three-terminal In_2Se_3 FE FETs mimicking synaptic behavior. The gate can be excited with optical stimuli. **f** Paired-pulse facilitation index of α- In_2Se_3/SnSe based p–n junctions as a function of optical pulse interval time (Δt). The fitted curve shows that PPF decreases exponentially with the increase of Δt. The inset displays postsynaptic current triggered by two consecutive optical pulses. **g** Schematic of reconfigurable graphene/$MoTe_2$/P(VDF-TrFE) homojunctions. The P(VDF-TrFE) layer independently controls ferroelectric domains, resulting in reversible p-n and n-p transitions. **h** Schematic of 3R MoS2 sliding-ferroelectric FETs, where shear-transformation in 3R MoS_2 epilayers induces polarization switching. **i** Schematic of bilayer graphene/h-BN based moiré synapse transistors, which exploit electronic ratcheting states generated by moiré potential to enable non-volatile conductance modulation. **j** Retention characteristics of In_2Se_3 FE FETs, showing high- and low-resistance states (HRS/LRS) under ±10 V write/erase pulses for 30 s, with readout at $V_{gs} = 0$ V, $V_{ds} = 1$ V. **k** Schematic of a lane-keeping task, where a laser sensor observes obstacle distance and inputs data into a reservoir computing network. The network output adjusts the vehicle's steering angle. Benchmark comparison of the 2D FE devices for ISC applications: **l** Energy consumption vs. retention time, **m** Sensing optical wavelength vs. operating voltage. Reproduced with permission from: **e**, **j**, **k** ref. 56, 2024 American Chemical Society; **f** ref. 35, John Wiley & Sons; **g** ref. 38, Springer Nature; **h** ref. 75, Springer Nature; **i** ref. 77, Springer Nature.

Its direct bandgap (2.14 eV), high carrier mobilities (157 $cm^2 V^{-1} s^{-1}$ for holes, 74 $cm^2 V^{-1} s^{-1}$ for electrons), and efficient visible-light absorption underpin robust optoelectronic functionality[63,64]. For example, ion-liquid-gated MoSSe FETs demonstrate optoelectronic synaptic behaviors, achieving a PPF index of 190%[32]. This device mimics the human visual system's light adaptation: under mild illumination (450 nm, 1 s, 0.040 mW/cm^2), its current remains sub-threshold (<1.3 nA), while stronger light (450 nm, 1 s, 0.061 mW/cm^2) triggers overstimulation (1.44 nA), akin to retinal responses. Applying a −1 V pulse modulates synaptic weight by redistributing Li^+ ions in the electrolyte, reducing the current to 1.2 nA to restore stable vision. A 10-by-10 array of these devices is used to preprocess optical inputs in three steps. The array converts light stimuli into electrical signals through MoSSe's visible-light absorption. A thresholding mechanism (1.09 nA) filters out noise by suppressing weak signals, akin to retinal neurons discarding subcritical inputs. The retained signals undergo contrast enhancement, sharpening edges and improving feature resolution. By integrating transduction, noise filtering, and contrast amplification, the system enhances data quality, boosting digit recognition accuracy from 77.6% to 83.3%.

2D interfacial FE devices combine 2D materials as channels with 3D FE materials as gate dielectrics, integrating high optoelectronic sensitivity, robust non-volatile memory, and long-term retention (>90,000 s) for energy-efficient ISC[38,50,65]. For instance, graphene/$MoTe_2$/P(VDF-TrFE) homojunctions employ split gates beneath the FE dielectric to independently control ferroelectric domains on either side of the devices[38] (Fig. 2g). By modulating these domains, the potential profile of homojunction can be reversibly tuned from p–n (negative photoresponsivity) to n-p (positive photoresponsivity), enabling multi-level synaptic weight tuning and photoresponsivity reversal. This functionality enables applications like reconfigurable convolutional kernels for edge detection. The devices demonstrate exceptional endurance (>10^6 cycles) and scalability into functional arrays. A 3-by-3 array of these devices operates as an artificial neural network (ANN), performing energy-efficient pattern recognition (10^{-13} J per operation) and

enabling real-time robotic control, such as directing a robotic dog to execute assigned tasks.

In addition to traditional 3D ferroelectrics such as BTO and P(VDF-TrFE), recently developed ferroelectric thin films like HfO_2 and $Hf_xZr_{1-x}O_2$ (HZO) have gained prominence due to their intrinsic scalability, CMOS compatibility[66,67] and robust ferroelectric behavior down to sub-10 nm thicknesses[68]. When integrated with 2D semiconductors such as MoS_2 and WSe_2, these films enable the realization of steep-slope FE-FETs for in-sensor memory and neuromorphic operations[69,70]. MoS_2/HZO-based FE-FETs show potential in ISC by demonstrating subthreshold swings below 60 mV/dec and energy-efficient synaptic behavior with sub-picojoule consumption per spike, along with fast switching (~4.8 ns), high retention (>10 years), and exceptional endurance (>10^{13} cycles)[71].

2D interlayer ferroelectricity originates from charge redistribution via the hybridization of occupied and unoccupied states or net charge transfer across van der Waals (vdW) interfaces, as observed in bilayers of h-BN[72] and transition metal dichalcogenides (TMDCs)[73,74]. 2D interlayer FE devices utilize emergent ferroelectricity phases formed by stacking 2D materials together. These new phases offer exceptional properties such as fast switching speeds, high endurance and low energy consumption at room temperature[75]. For example, h-BN/MoS_2/graphene transistors use shear transformation to induce polarity switching in 3R MoS_2 epilayers, meeting the sub-3 nm node requirement for future CMOS technologies (Fig. 2h). Graphene/bilayer h-BN based Fe-FETs employ ferroelectricity arising from parallel-stacked bilayer h-BN, demonstrating nanosecond switching speed and endurance exceeding 10^{11} cycles[76]. Bilayer graphene/h-BN moiré synapse transistors[77] (Fig. 2i) utilize excitonic ferroelectricity[52,78] arising from asymmetric moiré structure, operating at low-power (20 pW) while enabling diverse neuromorphic computing functionalities such as reconfigurable synaptic responses and input-specific adaptation. The moiré synapse transistors exploit electronic ratcheting states generated by moiré potential to enable non-volatile conductance modulation. In addition to the memory functionality, Moiré structures demonstrate intelligent light sensing capabilities. The photodetectors based on 1.2° twisted double bilayer graphene demonstrate bulk photovoltaic effect (3.7 V W^{-1}) at mid-infrared wavelengths (5 μm and 7.5 μm), due to symmetry breaking and quantum geometry contributions[79]. The bulk photovoltaic effect is electrically tunable and enables detection of light polarization, power and wavelength. By integrating memory, computing and sensing functionalities, 2D interlayer FE devices hold promise for ISC applications.

2D FE devices have demonstrated a broad range of ISC applications, including sociative learning[34,35], light adaptation[32], digit recognition[36,57] and edge detection[39]. These applications are achieved through individual ISC devices[35] or array-based configurations implementing computing architectures such as ANN[33], spiking neural networks[80] and RC systems[34]. For instance, in RC systems, In_2Se_3-based Fe-FETs, which exhibit a retention time exceeding 48 h (Fig. 2j), are employed to control the motion of robotic vehicles[56]. The vehicles are equipped with lidars to detect the obstacles, which serve as the input to network. The RC system processes input and dynamically adjust steer angle of the vehicles, leading to smooth lane navigation and temporal signal processing (Fig. 2k). The approach operates at 10^4 times lower power and achieves 25% higher data throughput per second compared to conventional GPU-based systems.

We benchmarked various 2D FE devices for ISC applications, as shown in Fig. 2l, m, evaluating key metrics such as energy consumption, retention time, sensing wavelength, and operating voltage. Energy per switching event was calculated using E = V·I·t, based on reported voltage, current, and pulse duration, unless the original study provided a measured value directly. Retention, wavelength, and voltage values were extracted from published data; where precise values were unavailable, we estimated typical values from average data or figure interpretations. Variations across studies are expected due to differences in device architecture, material quality, fabrication processes, and measurement setups. These benchmarks show that 2D ferroelectric ISC devices generally exhibit low operating voltages and excellent retention times, although switching energy can be relatively high due to polarization thresholds. The data also reveal clear trade-offs: devices such as Gr/$MoTe_2$/P(VDF-TrFE) achieve ultralow energy consumption (~10^{-13} J) with solid retention but require higher voltages (>10 V), while systems like WSe_2/In_2Se_3 offer broad spectral sensitivity (~600–1900 nm) but show limit retention time (~10^2 s). Overall, low-power-optimized platforms tend to operate at higher voltage costs, while broadband or high-retention systems may sacrifice endurance.

Memristor and memristive devices

Memristors and memristive devices are components whose resistance depends on the history of applied voltage or current, allowing them to store information as resistance states[81]. 2D memristor and memristive devices[82] enable multimodal and energy-efficient ISC by achieving non-volatile multiple memory states in response to external stimuli such as voltage, light, temperature, or mechanical stress[83]. Based on the resistance switching (RS) mechanisms, 2D memristor and memristive ISC devices are classified into three types: conductive filament, charge trapping and phase transition[84].

2D conductive filament devices leverage 2D materials as switching layers to achieve multiple resistance states by dynamically modulating the dimension of filaments[85]. The filaments are formed via metal ion migration (e.g., Ag^+, Cu^{2+}), or oxygen vacancy redistribution. Emerging 2D materials such as MXene-ZnO composites[86] and oxidized black phosphorus (BP)[87] enable multimodal ISC applications by integrating memristive switching with multimodal sensing capabilities of light, humidity, and strain. For instance, MXene-ZnO memristors (Fig. 3a) utilize UV light to tune oxygen vacancies and humidity to alter proton coupling (Fig. 3b), facilitating noise-reduced, environment-adaptive neuromorphic data preprocesses that accelerate training processes by 5 times[86]. Similarly, MXene-based piezo-resistive memristors detect mechanical stress with high sensitivity (23.9 kPa^{-1}) and broad range (>100 kPa), where pressure adjusts filament dimensions for multilevel switching[23]. These devices enable real-time Morse code recognition by encoding "dots" and "dashes" through dynamic and static pressures, respectively. The pressure signals alter the resistance states of the memristors, which store and process the signals. Excitatory post-synaptic currents decode the changes in resistance into alphanumeric outputs, facilitating Morse code interpretation without external conversion circuits.

2D charge trapping devices achieve multilevel non-volatile resistance states by modulating charge trapping at defect sites, 2D-2D/dielectric interfaces, or gate dielectrics, while leveraging the optoelectronic properties of 2D materials for high-sensitivity, high-endurance ISC applications[88–91]. For example, MoS_2-based memtransistors detect light at ultralow intensities (0.001 mW/cm^2) and endure >5 × 10^8 cycles, enabling secure data encryption via wafer-scale arrays of MoS_2 memtransistor[92] (Fig. 3c). These systems encode light signals into encrypted data through photosensitive analog programming, resisting eavesdropping and brute-force attacks while operating at ultra-low energy (~100 pJ/operation). An integrated 2D SnS-based memristor circuit demonstrates optoelectronic RC, where spatio-temporal electrical and optical inputs generate high-dimensional reservoir states. The optoelectronic RC maps complex temporal inputs into high-dimensional reservoir states, achieving 91% accuracy in classifying practical sentences with minor natural errors. The 2D h-BN/WSe_2 heterostructure offers enhanced properties for optical synapses[41]. The integrated optical sensor detects light in the 405–655 nm range, while the charge-trapping memristor controls synaptic weight. Light reduces the resistance of sensors, increasing carrier density in WSe_2 and enhancing charge trapping in the weight control layer to tune synaptic dynamics. The synapse devices form an ANN architecture which is capable of >90% accuracy in colored and color-mixed pattern recognition.

2D phase transition devices utilize resistance variations between distinct material phases to achieve multilevel non-volatile memory states, offering gigahertz response, multimodal sensing, and ultrahigh endurance for ISC[19]. For instance, VO_2-based memtransistors sensor both UV and visible light (Fig. 3d), inducing RS with long retention (>4000 s)[93]. Their distinct responses to UV and visible light enable RGB noise reduction in

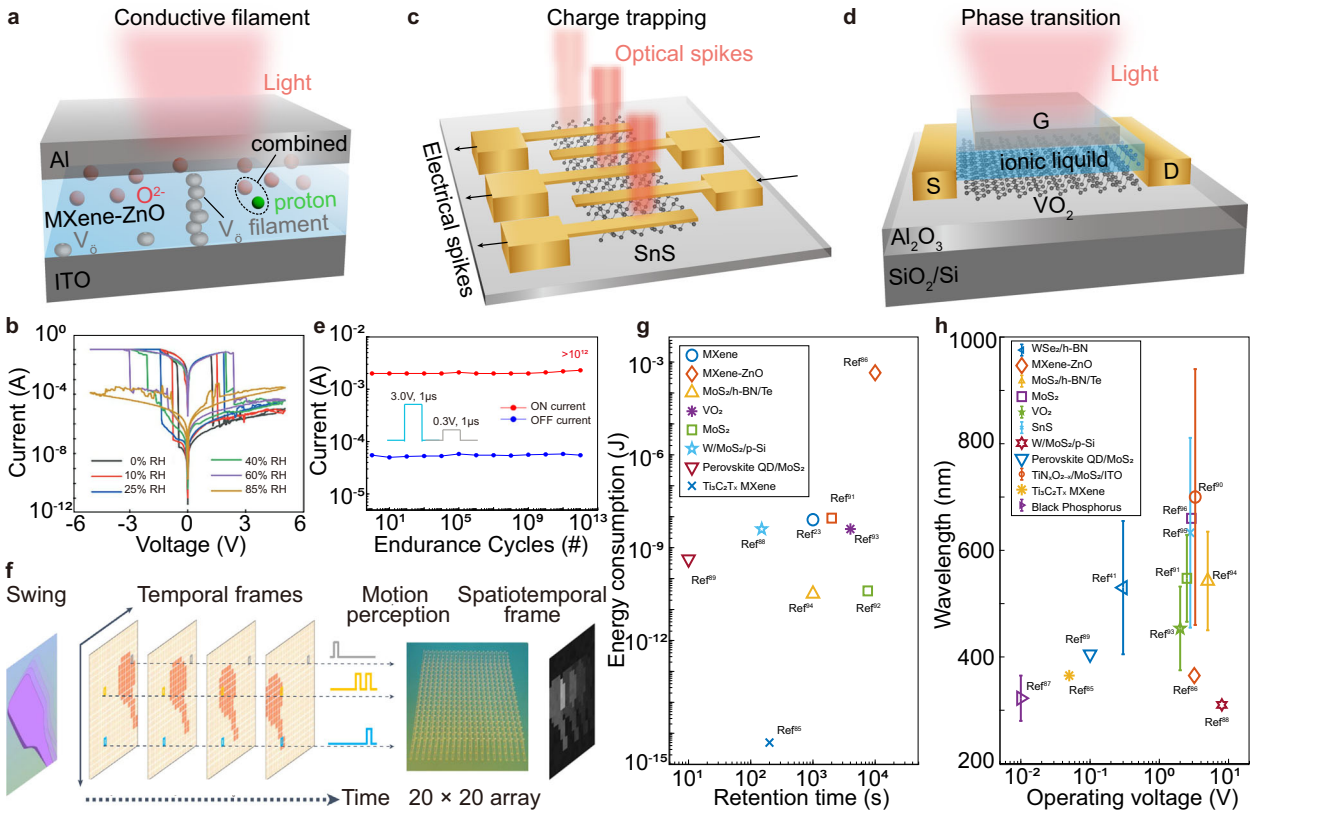

Fig. 3 | 2D memristors and memristive devices for in-sensor computing. **a** Schematic of MXene-ZnO-based flexible memristive devices with dual sensing capabilities for light and humidity. The resistance is modulated by formation of oxygen vacancy ($V_ö$) filament. Humidity influences resistance by introducing protons (H^+) that interact with oxygen ions (O^{2-}) and $V_ö$[86]. **b** I–V characteristics of MXene-ZnO memristors under varying relative humidity (RH) conditions, showing changes in resistive switching behavior. **c** Schematic of a multifunctional SnS-based memristor array, responsive to electrical and optical stimuli[95]. **d** Schematic of a VO_2-based neuromorphic transistor stimulated by 375 nm UV light, where the VO_2 film serves as a channel between source (S) and drain (D) electrodes, with ionic liquid as the gating medium[93]. **e** Endurance characteristics of a VO_2-based memristor, showing no signal degradation over 10^{12} cycles, using 3.0 V/1 μs write pulses and 0.5 V/1 μs erase pulses. **f** Schematic of MoS_2 phototransistor arrays for spatio-temporal vision sensing, visualizing motion through a sequence of temporal frames. Pixels from specific columns form a temporal vision sequence s(t), which is processed into temporal compressive states x(t), mimicking bioinspired vision sensors. Benchmark comparison of the 2D memristors and memristive devices for ISC applications: **g** Energy consumption vs. retention time, **h** Sensing optical wavelength vs. operating voltage. Reproduced with permission from: **b** ref. 86, John Wiley & Sons; **e** ref. 19, Springer Nature; **f** ref. 96, Springer Nature.

digit image preprocessing. Initially, the recognition accuracy was 24% due to noise from random Gaussian interference, which masked key features. After preprocessing with VO_2 memtransistors, which emphasize UV-specific information, the system filtered out the noise and extracted relevant features more effectively, boosting the accuracy to 93%. Additionally, atomically thin VO_2 films—which undergo light- and temperature-driven metal-to-insulator transitions—enable cross-modal spiking sensory neurons[19] with high endurance over 10^{12} cycles (Fig. 3e). These devices integrate VO_2 memristors with pressure sensors to encode pressure and temperature signals, enabling robotic hands to dynamically grasp or release objects (e.g., balls, hot water cups) with low latency (<30 ns).

2D memristors and memristive devices enable diverse ISC applications —such as associative learning[89], pattern recognition[94], data encryption[92], language learning[95], and human-machine interaction[19]—by leveraging multimodal sensing and ultralow energy consumption. A notable example is MoS_2 memtransistor-based optoelectronic graded neurons deployed in a two-stream neural network for motion detection and action recognition[96] (Fig. 3f). The spatial stream processes static frames for image recognition, while the temporal stream analyzes motion information to perceive object direction and visual saliency. This dual architecture achieves 99.2% recognition accuracy with a temporal resolution spanning 10^1–10^6 milliseconds, enabling real-time tracking of dynamic environments.

In comparison with conventional memristive technologies, 2D-material-based devices exhibit unique functional advantages but also face maturity-related challenges. Metal-oxide memristors, such as those based on TiO_2 and HfO_2, are well-established and offer high endurance (>10^9 cycles), fast switching (<10 ns), and robust integration with CMOS platforms, making them commercially viable for resistive memory and neuromorphic arrays [97,98]. Yet, these systems typically operate as isolated memory elements and are limited to electrical input[99]. Organic memristors, in contrast, feature mechanical flexibility, solution-processability, and low switching energy (<1 pJ), which are attractive for wearable computing and bioelectronics[100]. Yet, their limited environmental stability and short retention time restrict long-term deployment [101]. Compared to both, 2D memristors strike a compelling balance: they combine atomic-scale thickness and tunability via external stimuli making them promise for ISC. Nevertheless, their current limitations, including device-to-device variability, scalability, and endurance, must be addressed before they reach technological maturity.

We benchmarked various 2D memristor and memristive devices for ISC applications, as shown in Fig. 3g, h, assessing the same critical performance metrics such as energy consumption, retention time, sensing wavelength, and operating voltage as in Section “Ferroelectric devices”. Variations reflect differences in switching mechanisms, material quality, and device structure. The results show clear trade-offs. $Ti_3C_2T_x$ MXene achieves the lowest energy consumption (~10^{-15} J), with moderate retention (~10^2 s), suitable for low-power sensing. MXene-ZnO shows much higher energy (~10^{-3} J) but long retention (>10^4 s), favoring memory stability.

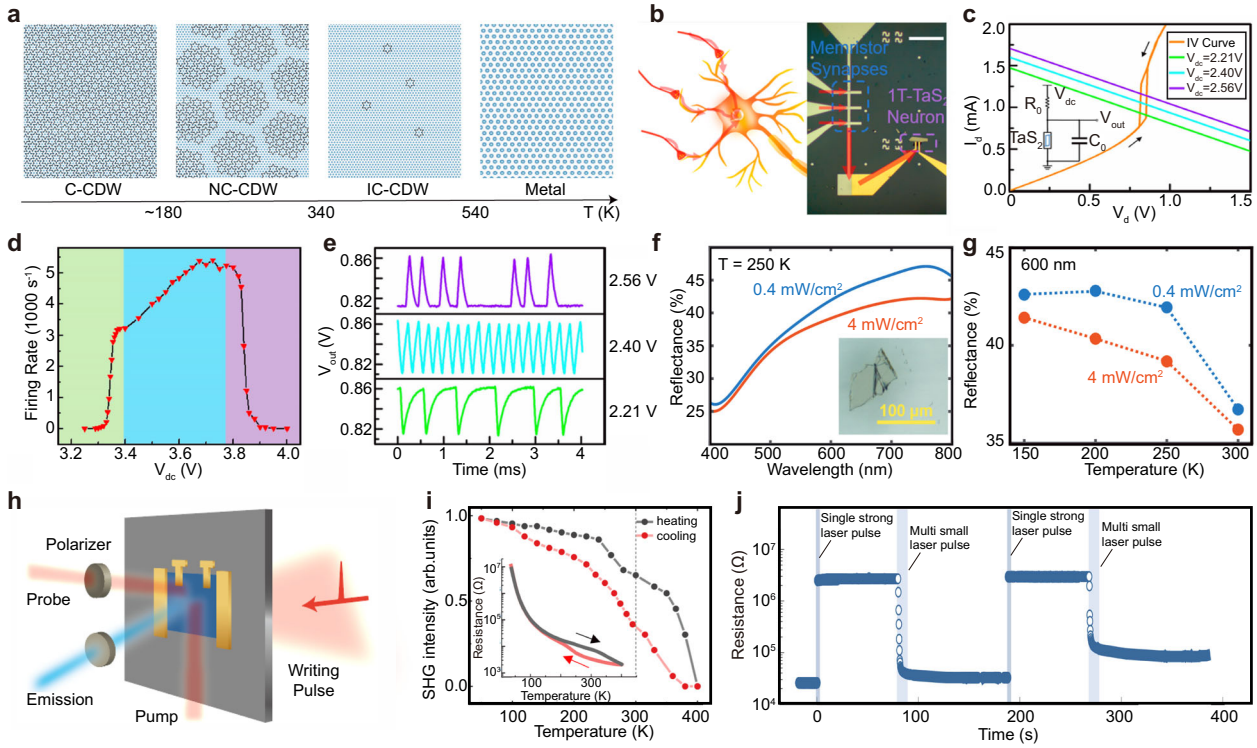

Fig. 4 | 2D charge density wave devices for in-sensor computing. a Phase transitions in 1T-TaS_2 at different temperatures, showing the commensurate CDW (CCDW, <180 K), nearly commensurate CDW (NCCDW, 180K–340 K), incommensurate CDW (ICCDW, 340K–540 K), and metallic (>540 K) phases. **b** Artificial neuronal devices based on 1T-TaS_2. Optical micrograph of a 3-synapse-1-neuron network, where three memristors are connected in parallel to a 1T-TaS_2 device, mimicking biological neurons. Scale bar: 100 μm. **c** I−V characteristics of the 1T-TaS_2 film, showing oscillator circuit behavior. Oscillations occur when V_{dc} is within 2.21 V (green line) to 2.56 V (violet line). **d** Firing rate vs. V_{dc} for the 1T-TaS_2-based neuronal oscillator, with a 3 kΩ series resistor, showing nonlinear behavior. **e** Oscillation waveforms corresponding to different V_{dc} values in (**c**). At V_{dc} = 2.21 V (green) and 2.56 V (violet), oscillations occur irregularly. At V_{dc} = 2.40 V (cyan), continuous oscillations are observed. **f** Reflectance spectra of 1T-TaS_2 under 0.4 mW/cm^2 and 4 mW/cm^2 incoherent white light illumination at 250 K. Inset: Optical image of a 1T-TaS_2 film (~100 μm). **g** Temperature-dependent reflectance of 1T-TaS_2 at 600 nm. Maximum optical tunability occurs around 250 K. **h** Schematic of the experimental setup for photo-manipulation of the polar electronic state in $EuTe_4$, using an 800 nm pump-probe system and a photomultiplier tube (PMT) for detection. **i** Temperature dependence of second-harmonic generation (SHG) intensity in pristine $EuTe_4$. A thermal hysteresis is observed, matching the hysteresis in the resistance curve (inset), indicating phase transition behavior. **j** Non-volatile switching of SHG intensity and resistance induced by high-intensity laser pulses. Strong excitation above the threshold fluence drives $EuTe_4$ into a new non-volatile phase, resulting in sharp resistance switching. Reproduced with permission from: **a** ref. 216, 2024 IOP Publishing; **b**–**e** ref. 112, 2021 American Chemical Society; **f**, **g** ref. 113, 2025 AIP Publishing LLC; **h**–**j** ref. 122, Springer Nature.

MoS_2-based heterostructures offer balanced performance. In Fig. 3h, most devices sense in the 300–900 nm range. TiN_xO_{2-x}/MoS_2/ITO and SnS provide broad spectral coverage but operate at higher voltages (>1 V), while Black Phosphorus and $Ti_3C_2T_x$ MXene achieve similar response under <1 V. Overall, devices with broader wavelength sensitivity tend to require higher voltages, while low-voltage systems offer narrower spectral windows.

Charge density wave devices

CDWs are collective electronic states characterized by periodic modulations in electron density, often coupled with lattice distortions, forming phases distinct from conventional metals or insulators[102,103]. These phenomena are observed in 2D TMDCs such as 1T-TaS_2[104], 1T-$TaSe_2$[105], 2H-$NbSe_2$[106], and 1T-VSe_2[107]. As temperature increases, CDWs transition between phases—commensurate (C-CDW), nearly commensurate (NC-CDW), and incommensurate (I-CDW)—each with distinct electronic ordering[108] (Fig. 4a). CDW phase transitions induce RS, enabling their use in ultrafast memory devices with picosecond-scale switching speeds and ultralow energy consumption (few femtojoules per operation)[109].

1T-TaS_2, a prototypical 2D CDW material, is widely studied for neuromorphic computing. 1T-TaS2 exhibits phase transitions from NC-CDW to C-CDW at room temperature through thermal or electric field stimuli[110,111]. The phase transition leads to 1T-TaS_2-based stochastic artificial neurons[112] (Fig. 4b), where a Pearson-Anson oscillator circuit is used to generate voltage-dependent oscillations ranging from 500 Hz to 5000 Hz. In the regular oscillation regime (Fig. 4c, blue region), increasing DC voltage (V_{dc}) enhances RC dynamics, elevating firing rates. Conversely, in stochastic regimes (green/purple), firing rates exhibit abrupt sensitivity to V_{dc} shifts (ΔV < 0.1 V) (Fig. 4d). Oscillation waveforms are tunable: low (2.21 V) and high (2.56 V) V_{dc} stabilize NC-CDW or IC-CDW phases, while intermediate voltages (2.40 V, cyan) induce stable oscillations (Fig. 4e), showcasing 1T-TaS_2's potential for reconfigurable stochastic neuron circuits. Additionally, optically tunable CDW domains in 1T-TaS_2 enable light-responsive (Fig. 4f) and temperature-responsive sensors[113,114] (Fig. 4g), bridging CDW physics with adaptive optoelectronic properties for ISC.

Recent studies have expanded 1T-TaS_2's functionality across multiple ISC-relevant domains. Optical excitation has been shown to induce a metastable heterochiral CDW state with coexisting α and β domains. These form a moiré superstructure with 43.7 Å periodicity and Kagome-like symmetry, resulting in emergent metallicity and flat bands near EF—features promising for ultrafast, light-reconfigurable memory[115]. In heterostructures, proximity-induced CDWs have been observed in graphene atop 1T-TaS_2, accompanied by a ~31% reduction in the Mott gap and a ~0.3 eV Dirac point shift, suggesting tunable hybrid electronic states[116]. At the system level, coupled oscillator arrays based on CDW quantum oscillators (CDW-QOs) have demonstrated second-harmonic injection locking and Ising spin encoding. These networks solve Max-Cut optimization problems in under 10 μs at room temperature, with low-voltage operation (~0.01 V) and frequency tunability from 195 to 537 kHz[117].

$EuTe_4$, an emerging quasi-2D CDW material[118], exhibits improper polarization enabled by its unique crystal structure[119]: planar Te-sheets separated by insulating EuTe slabs. CDW formation breaks in-plane inversion symmetry within the Te-sheets, inducing a polar order. The material hosts a ~200 meV CDW gap with incommensurate wave vectors along multiple directions, and a primary modulation ($q \approx 0.643$ b*) stable up to 400 K[120]. Scattering and STM measurements reveal competing trimerized domains with opposite polarizations, contributing to a wide thermal hysteresis between 50 K and 400 K and enabling domain-based memory retention[121].

Recent studies demonstrate that light pulses (800 nm) can non-volatilely manipulate the polar state and resistance of $EuTe_4$, as shown in Fig. 4h[122]. Pump-probe second harmonic generation (SHG) measurements (400 nm) track structural changes, while electrical resistance (measured via the four-electrode method) correlates with temperature-dependent SHG intensity, both displaying thermal hysteresis (Fig. 4i). Under strong excitation (~7.5 mJ/cm^2), $EuTe_4$ transitions to a high-resistance phase, whereas moderate pulses (~4.5 mJ/cm^2) fine-tune SHG intensity and restore resistance. Thermal annealing fully reverses the transition, resetting the system to its original state (Fig. 4j). This non-volatile, reversible optical control positions $EuTe_4$ as a promising candidate for adaptive optoelectronic memory. Additionally, $EuTe_4$ exhibits large negative magnetoresistance (~86%) at 2 K under magnetic fields above 4 T, attributed to spin canting of Eu^{2+} ions[120]. This behavior suggests that magnetic fields can modulate the CDW state, reinforcing $EuTe_4$'s potential as a reconfigurable platform for in-sensor memory systems driven by electric, optical, and magnetic inputs[123].

2D CDW systems have successfully demonstrated key in-sensor computing functionalities, including light- and temperature-responsive sensing[110,111,122], non-volatile memory through polar state switching[122], neuromorphic behavior[112] and coupled oscillator arrays[117]. These independent achievements establish a strong foundation for future ISC development. However, several challenges currently limit their practical deployment. Many CDW transitions occur below room temperature, with only a few materials (e.g., 1T-TaS_2, $EuTe_4$) exhibiting switching near ambient conditions[124]. Domain control is often difficult, as CDW phase switching involves metastable or hidden states that are highly sensitive to local structure and hard to program deterministically[125,126]. Ongoing efforts are being made to address these issues. For example, vdW heterostructures combining 1T-TaS_2 with graphene have been investigated to enable vertical transport and interlayer functionality[127], while h-BN-capped three-terminal CDW devices provide early demonstrations of gate tunability[128]. On the materials growth side, wafer-scale synthesis of monolayer 2H-$TaSe_2$ and TaS_2 films via APCVD has been reported[129,130], demonstrating a potential route to scalable integration.

Spintronic devices

2D materials exhibit different types of magnetism such as ferromagnetism, antiferromagnetism, ferrimagnetism and altermagnetism. Ferromagnetism originates from parallel alignment of atomic magnetic moments, driven by positive exchange interactions (Fig. 5a). 2D ferromagnetic (FM) materials like CrI_3[131], p-SnSe[132], VSe_2[133], and Fe_3GaTe_2[134], retain magnetization even without external fields. This inherent magnetization introduces challenges for high-density integration, as stray field coupling between adjacent magnetic domains can cause mutual interference, limiting scalability in ultra-compact spintronic devices[135]. Antiferromagnetism results from antiparallel spin alignment, canceling net magnetization via negative exchange interactions[136]. 2D antiferromagnetic (AFM) materials like $FePS_3$[137], $CuCrP_2S_6$[138], NiI_2[139] and $MnSe_2$[140] exhibit robust spin ordering with zero macroscopic magnetization(Fig. 5b). Ferrimagnetism arises from unequal antiparallel magnetic moments, resulting in a net magnetization. 2D ferrimagnets like Cr_2S_3[141] and supramolecular Kondo lattices[142] provide tunable spin properties with reduced stray field effects for spintronic manipulation[143]. Altermagnetism, a recently discovered class, uniquely combines compensated magnetic moments in real space with alternating spin splitting in momentum space[144,145] (Fig. 5c). This dual character enables spin-polarized currents without net magnetization, unlocking an extra spin degree of freedom for ISC paradigms. Emerging 2D altermagnetic (ALM) candidates include Mn_5Si_3 thin film[146], $Co_{1/4}NbSe_2$[147] and $Fe_{1/4}NbS_2$[148], host unprecedent spin alignment for spintronic applications.

Topological spin textures, such as skyrmions[149] and merons[150], transcend conventional magnetic order in 2D materials by organizing spins into stable, topologically protected configurations rather than simple parallel or antiparallel arrangements[151]. Skyrmions, nanoscale vortex-like spin structures, are stabilized by the interplay of dipolar interactions, Dzyaloshinskii-Moriya interactions (DMI)[152], and magnetic anisotropy[149](Fig. 5d). DMI is induced by broken inversion symmetry in chiral crystals or interfaces, driving the emergence of skyrmions in 2D systems. Examples include ultrathin metallic magnets (e.g., FeGe[153]), Cr-based vdW compounds (CrI_3[154], $CrGeTe_3$[155]), and heterostructures like h-BN/Co[156], $WTe_2/CrCl_3$[157] where interfacial DMI generates skyrmions that move and interact as particle-like entities with distinct dynamical modes. Merons, resembling half-skyrmions, exhibit partial spin winding and arise in materials such as $MnBr_2$[158] or strained twisted 2D magnets[159](Fig. 5e). Meron-based devices are promising for high storage density due to their nanoscale size[160]. These textures enable ultra-dense, low-energy spintronic devices, as their topological stability permits robust motion with minimal current[161].

2D spintronic devices harness the spin degree of freedom of electrons, leveraging magnetization dynamics, robust spin ordering, and topological stability in magnetic materials to manipulate electronic states and achieve tunable resistance[162]. The magnetoresistance effect inherent to these devices enables unique capabilities in magnetic field sensing for ISC. Traditional 2D spintronic devices include magnetic tunnel junctions (MTJs)[163] and multiferroic systems[164]. Emerging ALM order and topological spin textures enhance the performance of these systems, offering pathways to novel ISC devices with high-density memory and low-power operation[165].

MTJs are spintronic devices composed of two ferromagnetic layers separated by an ultrathin insulating tunneling barrier. These devices exploit tunneling magnetoresistance (TMR), where the relative magnetization alignment of the ferromagnetic layers governs the tunneling resistance, enabling non-volatile resistance switching. Two-dimensional materials such as h-BN and TMDCs (e.g., MoS_2 and WS_2) serve as atomically thin, smooth tunneling barriers, enhancing TMR ratios and scalability[166,167] (Fig. 5f). For the ferromagnetic layers, 2D vdW magnets like Fe_3GeTe_2, $Cr_2Ge_2Te_6$, and CrI_3 provide tunable magnetism, room-temperature ferromagnetic order, and robust spin filtering[168,169]. Beyond memory, MTJs enable novel computing paradigms such as probabilistic computing[170], where stochastic MTJs paired with 2D-MoS_2 FETs[171] realize "p-bits"— fluctuating units that harness intrinsic stochasticity— for tasks like random number generation and spin logic (Fig. 5h). MTJs exhibit magnetic field-sensing and strain-sensing capabilities (Fig. 5i), as their magnetization direction and free energy in the ferromagnetic layer are sensitive to applied stress, allowing tunable TMR for detecting strain amplitudes and direction[172,173]. The non-volatile memory and multimodal sensing capabilities make MTJs promise toward ISC applications.

2D multiferroic devices integrate sensing, memory, and processing functionalities into a single platform by exploiting tunable magnetoelectric coupling. These systems often employ heterostructures combining 2D magnetic materials (e.g., $Cr_2Ge_2Te_6$[174]) and ferroelectric layers (e.g., In_2Se_3), enabling reconfigurable spin-dependent optoelectronic responses[175] (Fig. 5g). For memory applications, the ferroelectric layer controls the magnetic state of the heterostructure, allowing nonvolatile data storage through reversible transitions between ferromagnetic (spin-polarized photocurrent, "1") and AFM (unpolarized photocurrent, "0") states[176] (Fig. 5j). Simultaneously, the spin-constrained photoelectric effect underpins their sensing capability: variations in light exposure modulate charge transfer and photocurrent characteristics, enabling optical readout of stored information without altering its magnetic state[176]. This dual functionality positions 2D multiferroics as promising candidates for ISC applications.

Altermagnetism enables spin current generation without spin–orbit coupling. In altermagnets, a charge current applied perpendicular to the

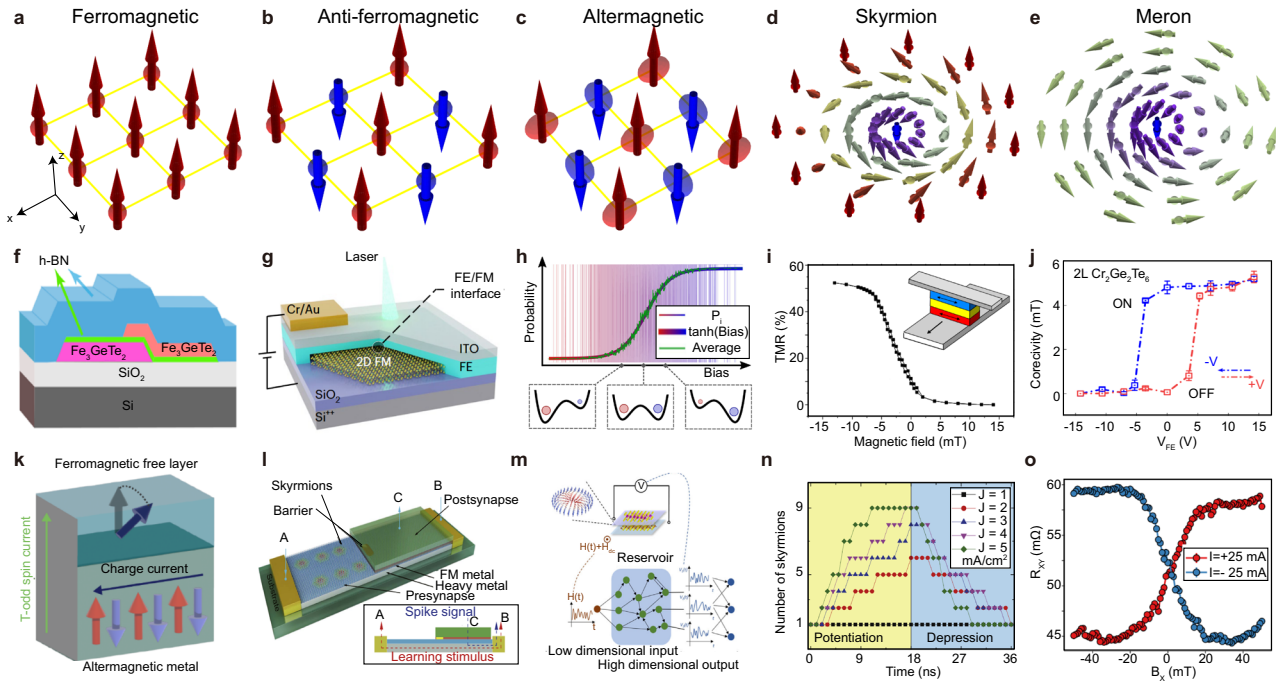

Fig. 5 | 2D spintronic devices for in-sensor computing. a–e Schematic of spin alignments in 2D magnetic systems: **a** Ferromagnetism: All spins align parallel, producing net magnetization. **b** Antiferromagnetism: Spins align in antiparallel sublattices, canceling net magnetization. **c** Altermagnetism: Antiparallel spin sublattices connected by crystallographic rotational symmetry (e.g., 2-fold, 4-fold, 6-fold), which are distinct from inversion, translation, or mirror symmetry. **d** Skyrmions: Topological spin textures with fixed chirality, where spins swirl continuously from "up" at the periphery to "down" at the core. **e** Merons: Half-skyrmion excitations where spins transition from in-plane orientations at the periphery to "down" at the core. **f** Schematic of a spin valve device using Fe_3GeTe_2 as the magnetic layer and h-BN as an insulating barrier. Thin Fe_3GeTe_2 layers (L1: ~7 nm, L2: ~20 nm) are separated by an atomically thin h-BN layer and encapsulated by a thicker h-BN layer. **g** Schematic of a $Cr_2Ge_2Te_6$/P(VDF-TrFE) multiferroic heterostructure, sandwiched between an ITO/Au top electrode and a SiO_2/Si substrate. **h** Probabilistic computing with p-bits, where bias voltage controls the probability distribution between two states. **i** Transfer curve of a perpendicular magnetic tunnel junction based on an AlO_x barrier, demonstrating magnetic sensing capabilities. **j** Voltage-dependent magnetic coercivity in a 2L-$Cr_2Ge_2Te_6$/P(VDF-TrFE) heterostructure at 4 K, showing coercivity modulation and memory functionality under different applied voltages. **k** Schematic of spin splitter torque devices, where spin polarization from altermagnetism flips the adjacent free ferromagnetic layer. **l** Schematic of a skyrmionic synaptic device, where bidirectional learning stimuli move skyrmions into (potentiation) or out of (depression) the postsynapse region, mimicking biological synapses. **m** Skyrmion-based neuromorphic computing concept, showing a Hall bar device and a magnetic skyrmion reservoir for computation. **n** Synaptic behavior of skyrmion-based devices, showing the number of skyrmions in the postsynapse during potentiation and depression modes under different learning stimulus densities. **o** Magnetic sensing using skyrmion devices, where transverse resistance (R_{xy}) evolves under an in-plane magnetic field (B_x) for positive and negative currents (±25 mA). Reproduced with permission from: **f** ref. 169, 2018 American Chemical Society; **g**, **j** ref. 174, Springer Nature; **h** ref. 170, 2025 AIP Publishing LLC; **i** ref. 217, 2025 IEEE; **k** ref. 144, 2025 American Chemical Society; **l**, **n** ref. 161, 2017 IOP Publishing Ltd; **m** ref. 183, 2025 American Association; **o** ref. 182, arxiv.

Néel vector generates a spin current parallel to it. This phenomenon, termed spin-splitter torque, provides a basis for new spintronic devices. Altermagnets provide a new mechanism for the generation of spin currents that do not rely on spin−orbit coupling, offering a mechanism termed spin splitter torque devices (Fig. 5k). Integrating ferroelectricity and ferromagnetism into a single material remains a significant challenge. Altermagnets provide a promising avenue for achieving such coexistence, as their unique spin-symmetry properties enable simultaneous ferroelectric and spin polarization. Recent experimental progress supports this potential: studies of (Ge, Mn)Te alloys, which span the phase diagram between FE GeTe and ALM MnTe, demonstrate tunable magnetoelectric coupling[177]. In 3D systems, large TMR has been predicted in MTJs with altermagnets theoretically[178,179], and also realized experimentally[180] at room temperature. This is due to the momentum dependent spin polarization even though the total density of states for spin-up and spin-up down electrons at the Fermi energy are the same in these unique materials. This intriguing effect has just emerged as a new frontier in the research of MTJs with 2D materials.

2D magnetic skyrmions, with their nanoscale size, defect tolerance, and ultralow depinning current density, are promising information carriers for ultra-dense, high-speed, and energy-efficient spintronic applications such as racetrack memories[181], logic gates, neuromorphic computing[161], and magnetic sensing[182] (Fig. 5l). For neuromorphic architectures, skyrmion-based devices like Pt/Co/Ir heterostructures leverage nonlinear magnetic field-driven dynamics in Hall bars to emulate reservoir computing[183] (Fig. 5m). Skyrmions act as reconfigurable processing units, enabling high-dimensional mapping and short-term memory effects (Fig. 5n). The devices demonstrate a skyrmion density-dependent accuracy (highest 94.7%) in handwritten digit recognition. Skyrmions show magnetic sensing capabilities: a $[W/CoFeB/MgO]_{10}$ multilayer Hall bar sensor exploits spin-orbit torque-induced transformations between skyrmions, stripe domains, and type-II bubbles[182]. By monitoring anomalous Hall effect signals via a differential readout scheme, it detects in-plane (±17 mT) and out-of-plane (±30 mT) fields with linear response and higher sensitivity over conventional anomalous Hall effect sensors (Fig. 5o).

CMOS compatibility remains a challenge for 2D spintronic ISC devices due to three key limitations: low thermal and chemical stability, poor interface quality, and limited synthesis scalability. Many 2D magnets, such as CrI_3 and $Cr_2Ge_2Te_6$, are air-sensitive and exhibit sub-room-temperature Curie points, requiring encapsulation and cryogenic operation incompatible with CMOS processes[131,184]. Approaches like strain engineering, chemical doping, and heterostructure design have shown promise in improving coercivity and thermal stability[185,186]. Notably, MBE-grown Fe_3GeTe_2 has demonstrated higher Curie temperatures and improved film uniformity[187]. Interface quality also remains a concern, as metal contacts (e.g., Pt, Ta) often introduce contamination and spin scattering[188,189]. Encapsulation with h-BN and other passivation methods help preserve interface integrity but remain

difficult to scale[186]. Meanwhile, wafer-scale synthesis of 2D magnets remains limited. Techniques such as CVD and mechanical exfoliation often yield defects and poor uniformity[190], which hinder reliable integration, especially in multilayer heterostructures where interface control and doping precision are critical[191].

Spintronic devices offer promising ISC capabilities, with MTJs enabling memory-in-sensor architectures[59,172], multiferroic devices supporting low-power spin logic[176], and skyrmion-based devices demonstrating magnetic sensing[182], and neuromorphic functions[183]. However, spintronic devices face several key challenges for ISC applications. Many 2D magnets suffer from low Curie temperatures and require cryogenic conditions, limiting practical deployment[162]. Interface quality in magnetic heterostructures is critical, as oxidation and defects degrade spin injections and suppress magnetoresistance signals[162]. Spintronic readout signals, such as TMR, are often weak and demand amplification or improved sensing architectures[192]. Scalability remains an issue: wafer-scale synthesis of uniform 2D magnets is difficult, and conventional spintronic devices face thermal stability and interface control challenges as dimensions shrink[20]. Recent efforts have begun addressing these issues. For example, vdW magnetic electrode transfer has enabled high-performance 2D spin valves with improved interface quality[193], while integrated multiferroic tunnel junctions using Mn_2Se_3, $TiTe_2$, and In_2S_3 have demonstrated in-memory logic and multilevel storage via magnetic and electric-field control[194].

Summary and outlook

Two-dimensional material-based ISC devices achieve their performance through fundamentally distinct physical mechanisms, each shaping how information is sensed, stored, and processed at the material level. FE devices utilize switchable polarization domains arising from broken crystal symmetry. These bistable dipole configurations can be flipped with low energy and minimal leakage, enabling fast, non-volatile operation and long retention[34]. Memristive devices operate via ion migration, filament formation, or phase transitions. Such localized and stimulus-responsive processes allow high-speed switching and multimodal sensing[19], but their variability and diffusion-driven mechanisms limit endurance and retention[86]. CDW systems exploit collective electron behavior, where the entire electronic structure reorganizes coherently[112]. This allows for femtojoule, picosecond transitions, ideal for neuromorphic oscillators and memory, though the metastable nature of CDW phases often complicates control and reproducibility. Spintronic devices rely on spin polarization[170], magnetic anisotropy[182], and topological textures such as skyrmions[195]. These enable non-volatile magnetoresistive states and vector-sensitive sensing[182], yet their performance is constrained by interface quality, temperature stability, and efficient spin injection. Each mechanism offers specific advantages while also introducing performance trade-offs.

Scaling up high-performance 2D ISC devices is essential for bridging the gap between laboratory innovations and practical real-world applications. Critical challenges span wafer-scale synthesis, defect-minimized transfer, and heterogeneous integration[17,196]. To address synthesis, techniques like chemical vapor deposition (CVD) and metal-organic CVD enable growth of uniform 2D transition metal dichalcogenides (TMDCs, e.g., MoS_2, WS_2) on 300-mm silicon wafers, compatible with back-end-of-line (BEOL) semiconductor processes[197]. Substrate engineering, such as step-controlled templates, further ensures single-crystal film uniformity. In addition, wafer-scale growth of single-domain 2D monolayer arrays via geometric confinement[198] and stacked multilayer vdW superconductors through a high-to-low temperature growth strategy[199] have been demonstrated. However, transferring these atomically thin layers to target substrates risks introducing defects or contamination, necessitating advanced transfer protocols (e.g., polymer-free methods) to preserve material integrity[200]. To address these issues, recent efforts have focused on (i) polymer-assisted wet transfer methods, (ii) polymer-free transfer methods, such as adhesive tape-based solvent-free transfer[201], and (iii) deterministic dry transfer methods[200]. High-throughput layer-by-layer exfoliation techniques have also been proposed for generating multiple compound semiconductor membranes from a single wafer[202]. For system-level integration, monolithic 3D architectures, where 2D material layers are sequentially stacked onto prefabricated silicon circuitry, offer a scalable path toward compact ISC systems. This approach enables vertical interconnects with minimized footprint while preserving the performance of bottom-tier CMOS logic, especially when combined with low-temperature transfer techniques and interlayer isolation strategies[16]. Monolithic 3D integration of 2D material-based AI-processing hardware has recently been demonstrated, highlighting integrability and multifunctionality[16]. However, challenges such as interlayer misalignment, interface contamination, and poor via connectivity need to be addressed to ensure layer-to-layer reliability[16,203].

Current 2D material-based ISC applications, such as digit recognition and edge detection, are constrained to either single-modality optical sensing or lack real-time data processing capabilities. Advancing toward complex applications like autonomous robotics[204] or wearable health monitoring[205] requires ISC systems to achieve multimodal integration and spatiotemporal analysis. Recent progress highlights a pathway[96]: motion-detection ISC systems based on MoS_2 memtransistors employ two-stream neural networks to decouple static spatial data (e.g., object shape) from dynamic temporal data (e.g., movement), leading to real-time action recognition.

Compared to conventional ISC platforms such as Si[42], ZnO[206], ITO[207],and organic semiconductors[208], 2D materials offer significant advantages in terms of energy efficiency, spectral coverage, and multimodal sensing versatility (Table 1), owing to their atomic thickness and high surface-to-volume ratio. While conventional systems benefit from mature fabrication processes, excellent endurance (>10^6 cycles), and reliable device integration, they typically suffer from higher energy consumption (10^{-6}–10^{-8} J) and limited sensing functionality, often restricted to visible light. In contrast, 2D ISC devices achieve ultralow switching energies (down to 10^{-13} J), broader spectral sensitivity (280–1310 nm), and support diverse inputs such as light, humidity, and pressure.

Emerging 2D topological insulators (TIs) enable ISC with unprecedented functionalities through their unique quantum properties: insulating bulk states and spin-polarized, topologically protected surface/edge states[209]. These states support phenomena like dynamic magnetoelectric effects, chiral edge transport, and the giant anomalous Hall effect[210], leading to adaptive sensing, low-power in-memory computing, and stable readout for probabilistic/neuromorphic architectures[211]. For example, magnetic TIs achieve high-accuracy pattern recognition at cryogenic temperatures[211]. Practical implementation is limited by low Curie temperatures, air sensitivity, and phase instability in candidate materials like $MnBi_2Te_4$[212,213]. To overcome these issues, recent work has explored capping strategies using Al_2O_3 or graphene to stabilize magnetic and topological phases at room temperature[214]. Topologically protected boundary states in 2D insulators enable high-mobility, backscattering-immune charge transport, which can enhance thermoelectric effects such as the Seebeck response. This supports thermoelectric-driven ISC applications, particularly in scenarios where efficient thermal management is critical[215].

2D ISC systems have the potential to significantly enhance biomedical applications that demand real-time, on-device processing of multimodal signals, such as brain-machine interfaces, seizure detection systems, and health monitoring platforms. Current 2D material-based systems have already demonstrated promising performance in these fields. For instance, in brain-machine interfaces, 2D systems enable real-time neural signal decoding with sub-millisecond latency and ultralow power consumption by processing electroencephalogram (EEG) and local field potentials directly at the sensor layer[25,26]. In seizure detection, on-chip 2D devices based on charge-trap memory and dynamic memristor arrays support real-time EEG analysis and closed-loop neuromodulation, achieving sub-second latency, nanowatt-level power consumption, and classification accuracies exceeding 96%[27,28]. In wearable health monitoring, 2D systems allow continuous, on-body tracking of signals such as glucose, temperature, and motion, with real-time response within milliseconds, low detection limits (e.g., <10 μM for glucose), and sub-microwatt power consumption[29,30]. ISC architectures that co-integrate sensing, memory, and computing at the sensor level could

Table 1 | Comparison of in-sensor computing devices based on conventional and 2D materials.

Materials	Sensory source	Application	Energy consumption (J)	Operating voltage (V)	Endurance (cycles)	Retention (s)	Light wavelength (nm)
Conventional materials							
ZnO/Ag/ITO [197]	Light	Face recognition	1.0×10^{-6}	2	500	1.0×10^{4}	white
Si [42]	Light	Edge computing	1.0×10^{-7}	2.5	$>1 \times 10^{3}$	–	650–950
CuPc/P(VDF-TrFE) [199]	Light	Pain formation simulation	4.6×10^{-8}	0.5	-	$>5.0 \times 10^{1}$	660, 445
ITO/SA Biopolymer [198]	Light	Pain perception	10^{-8} to 10^{-7}	2	>250	-	360–860
2D materials							
MoS_2/BTO [50]	Light	Digit recognition	1.8×10^{-12}	5	100	1.0×10^{5}	450–650
Gr/$MoTe_2$/P(VDF-TrFE) [38]	Light	Edge detection	1.0×10^{-13}	15	1×10^{6}	9.0×10^{4}	340–1310
α-In_2Se_3 (2H) [56]	Light	Lane keeping	2.7×10^{-7}	3	1×10^{4}	1.7×10^{5}	532
Black phosphorus [87]	Light	Pavlovian learning	9.2×10^{-10}	0.01	–	–	280–365
VO_2 (20 nm film) [93]	Light	Image recognition	4.0×10^{-8}	2	–	4.0×10^{3}	375–532
MXene–ZnO [86]	Humidity & Light	Image recognition	4.5×10^{-6}	3	–	1.0×10^{4}	365
VO_2 (40 nm film) [19]	Temperature & pressure	human machine interaction	3.9×10^{-9}	2	1×10^{12}	-	-
$Ti_3C_2T_x$ MXenes [85]	Light	Supervised learning	5×10^{-15}	0.05	>550	>200	365
MoSSe [32]	Light	Light adaptation	4×10^{-9}	4	>4000	>100	350–550
MoS_2/h-BN/Te [94]	Light	Dimensionality reduction	3.2×10^{-10}	5	1×10^{4}	$>1.0 \times 10^{3}$	450–635

further advance these systems by minimizing data transfer, lowering energy consumption, and shrinking device footprint.

The field of 2D ISC devices is rapidly evolving, driven by breakthroughs in new materials, device architectures, and integration strategies. Advances in ferroelectric, memristive, and spintronic 2D materials are pushing the boundaries of energy-efficient, multifunctional ISC, enabling real-time data processing and adaptive sensing. As research progresses, intelligent materials and sensors will seamlessly integrate with emerging technologies, accelerating the development of next-generation IoT and AI systems.

Data availability

No datasets were generated or analyzed during the current study.

Received: 24 March 2025; Accepted: 10 June 2025;
Published online: 04 August 2025

References

1. Li, S., Xu, L. D. & Zhao, S. The internet of things: a survey. *Inf. Syst. Front.* **17**, 243–259 (2015).
2. Das, S. & Mao, E. The global energy footprint of information and communication technology electronics in connected internet-of-things devices. *Sustain. Energy Grids Netw.* **24**, 100408 (2020).
3. O'Leary, D. E. Artificial intelligence and big data. *IEEE Intell. Syst.* **28**, 96–99 (2013).
4. Nahavandi, D., Alizadehsani, R., Khosravi, A. & Acharya, U. R. Application of artificial intelligence in wearable devices: opportunities and challenges. *Comput. Methods Prog. Biomed.* **213**, 106541 (2022).
5. Zhou, F. & Chai, Y. Near-sensor and in-sensor computing. *Nat. Electron.* **3**, 664–671 (2020).
6. Christensen, D. V. et al. 2022 roadmap on neuromorphic computing and engineering. *Neuromorph. Comput. Eng.* **2**, 22501 (2022).
7. Imran, M. A., Zoha, A., Zhang, L. & Abbasi, Q. H. Grand challenges in IoT and sensor networks. *Front. Commun. Netw.* **1**, 619452 (2020).
8. Zidan, M. A., Strachan, J. P. & Lu, W. D. The future of electronics based on memristive systems. *Nat. Electron.* **1**, 22–29 (2018).
9. Akarvardar, K. & Wong, H.-S. P. Technology prospects for data-intensive computing. *Proc. IEEE* **111**, 92–112 (2023).
10. Wan, T. et al. In-sensor computing: materials, devices, and integration technologies. *Adv. Mater.* **35**, 2203830 (2023).
11. Chen, C., Zhou, Y., Tong, L., Pang, Y. & Xu, J. Emerging 2D ferroelectric devices for In-sensor and In-memory computing. *Adv. Mater*. 2400332. https://doi.org/10.1002/adma.202400332 (2024).
12. Shi, Y., Duong, N. T. & Ang, K.-W. Emerging 2D materials hardware for in-sensor computing. *Nanoscale Horiz.* **10**, 205–229 (2025).
13. Hassan, J. Z. et al. 2D material-based sensing devices: an update. *J. Mater. Chem. A* **11**, 6016–6063 (2023).
14. Chen, M. et al. Selective and quasi-continuous switching of ferroelectric Chern insulator devices for neuromorphic computing. *Nat. Nanotechnol.* **19**, 962–969 (2024).
15. Zhu, K. et al. Hybrid 2D–CMOS microchips for memristive applications. *Nature* **618**, 57–62 (2023).
16. Kang, J.-H. et al. Monolithic 3D integration of 2D materials-based electronics towards ultimate edge computing solutions. *Nat. Mater.* **22**, 1470–1477 (2023).
17. Jayachandran, D., Sakib, N. U. & Das, S. 3D integration of 2D electronics. *Nat. Rev. Electr. Eng.* **1**, 300–316 (2024).
18. An, J. et al. Perspectives of 2D materials for optoelectronic integration. *Adv. Funct. Mater.* **32**, 2110119 (2022).
19. Li, Z. et al. Crossmodal sensory neurons based on high-performance flexible memristors for human-machine in-sensor computing system. *Nat. Commun.* **15**, 7275 (2024).
20. Zhang, B., Lu, P., Tabrizian, R., Feng, P. X.-L. & Wu, Y. 2D Magnetic heterostructures: spintronics and quantum future. *npj Spintron.* **2**, 6 (2024).
21. Cui, C., Xue, F., Hu, W.-J. & Li, L.-J. Two-dimensional materials with piezoelectric and ferroelectric functionalities. *npj 2D Mater. Appl.* **2**, 18 (2018).
22. Shin, Y. et al. Ultrasensitive multimodal tactile sensors with skin-inspired microstructures through localized ferroelectric polarization. *Adv. Sci.* **9**, 2105423 (2022).
23. Huang, J. et al. A bioinspired MXene-based flexible sensory neuron for tactile near-sensor computing. *Nano Energy* **126**, 109684 (2024).
24. Subbulakshmi Radhakrishnan, S., Sebastian, A., Oberoi, A., Das, S. & Das, S. A biomimetic neural encoder for spiking neural network. *Nat. Commun.* **12**, 2143 (2021).

25. Kostarelos, K., Vincent, M., Hebert, C. & Garrido, J. A. Graphene in the design and engineering of next-generation neural interfaces. *Adv. Mater.* **29**, 1700909 (2017).
26. Faisal, S. N. & Iacopi, F. Thin-film electrodes based on two-dimensional nanomaterials for neural interfaces. *ACS Appl. Nano Mater.* **5**, 10137–10150 (2022).
27. Yang, Z. et al. Seizure detection using dynamic memristor-based reservoir computing and leaky integrate-and-fire neuron for post-processing. *APL Mach. Learn*. **1**, 046123 (2023).
28. Farronato, M. et al. Seizure detection via reservoir computing in MoS_2-based charge trap memory devices. *Sci. Adv*. **11**, eadr3241 (2025).
29. Tyagi, D. et al. Recent advances in two-dimensional-material-based sensing technology toward health and environmental monitoring applications. *Nanoscale* **12**, 3535–3559 (2020).
30. Kumar Gupta, V., Choudhary, K. & Kumar, S. Two-dimensional materials-based plasmonic sensors for health monitoring systems —a review. *IEEE Sens. J.* **23**, 11324–11335 (2023).
31. Du, L. et al. Moiré photonics and optoelectronics. *Science* **379**, eadg0014 (2023).
32. Meng, J. et al. Integrated In-sensor computing optoelectronic device for environment-adaptable artificial retina perception application. *Nano Lett.* **22**, 81–89 (2022).
33. Das, B. et al. Artificial visual systems fabricated with ferroelectric van der waals heterostructure for in-memory computing applications. *ACS Nano* **17**, 21297–21306 (2023).
34. Wang, P. et al. Integrated In-memory sensor and computing of artificial vision based on full-vdW optoelectronic ferroelectric field-effect transistor. *Adv. Sci.* **11**, 2305679 (2024).
35. Ci, W. et al. All-In-one optoelectronic neuristor based on full-vdW two-terminal ferroelectric p–n heterojunction. *Adv. Funct. Mater.* **34**, 2305822 (2024).
36. Liu, K. et al. An optoelectronic synapse based on α-In2Se3 with controllable temporal dynamics for multimode and multiscale reservoir computing. *Nat. Electron* **5**, 761–773 (2022).
37. Zha, J. et al. Electronic/optoelectronic memory device enabled by tellurium-based 2D van der Waals heterostructure for in-sensor reservoir computing at the optical communication band. *Adv. Mater.* **35**, 2211598 (2023).
38. Wu, G. et al. Ferroelectric-defined reconfigurable homojunctions for in-memory sensing and computing. *Nat. Mater.* **22**, 1499–1506 (2023).
39. Zeng, J. et al. Multisensory ferroelectric semiconductor synapse for neuromorphic computing. *Adv. Funct. Mater.* **34**, 2313010 (2024).
40. Li, X. et al. Multi-functional platform for in-memory computing and sensing based on 2D ferroelectric semiconductor α-In_2 Se_3. *Adv. Funct. Mater.* **34**, 2306486 (2024).
41. Seo, S. et al. Artificial optic-neural synapse for colored and color-mixed pattern recognition. *Nat. Commun.* **9**, 5106 (2018).
42. Choi, C. et al. Reconfigurable heterogeneous integration using stackable chips with embedded artificial intelligence. *Nat. Electron* **5**, 386–393 (2022).
43. Leblanc, C., Song, S. & Jariwala, D. 2D ferroelectrics and ferroelectrics with 2D: materials and device prospects. *Curr. Opin. Solid State Mater. Sci.* **32**, 101178 (2024).
44. Wang, H. et al. The evolution of 2D vdW ferroelectric materials: theoretical prediction, experiment confirmation, applications. *Appl. Phys. Rev.* **11**, 21330 (2024).
45. Scott, J. F. Applications of modern ferroelectrics. *Science* **315**, 954–959 (2007).
46. Xue, F. et al. Room-temperature ferroelectricity in hexagonally layered α-In_2 Se_3 nanoflakes down to the monolayer limit. *Adv. Funct. Mater.* **28**, 1803738 (2018).
47. Higashitarumizu, N. et al. Purely in-plane ferroelectricity in monolayer SnS at room temperature. *Nat. Commun.* **11**, 2428 (2020).
48. Chang, K. et al. Microscopic manipulation of ferroelectric domains in SnSe monolayers at room temperature. *Nano Lett.* **20**, 6590–6597 (2020).
49. Liu, F. et al. Room-temperature ferroelectricity in CuInP2S6 ultrathin flakes. *Nat. Commun.* **7**, 12357 (2016).
50. Du, J. et al. A robust neuromorphic vision sensor with optical control of ferroelectric switching. *Nano Energy* **89**, 106439 (2021).
51. Sui, F. et al. Sliding ferroelectricity in van der Waals layered γ-InSe semiconductor. *Nat. Commun.* **14**, 36 (2023).
52. Zheng, Z. et al. Unconventional ferroelectricity in moiré heterostructures. *Nature* **588**, 71–76 (2020).
53. Xiao, J. et al. Intrinsic two-dimensional ferroelectricity with dipole locking. *Phys. Rev. Lett.* **120**, 227601 (2018).
54. Dutta, D., Mukherjee, S., Uzhansky, M. & Koren, E. Cross-field optoelectronic modulation via inter-coupled ferroelectricity in 2D In2Se3. *npj 2D Mater. Appl* **5**, 81 (2021).
55. Li, X., Li, S., Tang, B., Liao, J. & Chen, Q. A Vis-SWIR photonic synapse with low power consumption based on WSe_2 /In_2 Se_3 ferroelectric heterostructure. *Adv. Electron. Mater.* **8**, 2200343 (2022).
56. Zhou, J. et al. Multimodal 2D ferroelectric transistor with integrated perception-and-computing-in-memory functions for reservoir computing. *Nano Lett*. acs.nanolett.4c05071. https://doi.org/10.1021/acs.nanolett.4c05071 (2024).
57. Duong, N. T. et al. Coupled ferroelectric-photonic memory in a retinomorphic hardware for In-sensor computing. *Adv. Sci.* **11**, 2303447 (2024).
58. Wang, X. et al. Van der Waals engineering of ferroelectric heterostructures for long-retention memory. *Nat. Commun.* **12**, 1109 (2021).
59. Wu, J. et al. High tunnelling electroresistance in a ferroelectric van der waals heterojunction via giant barrier height modulation. *Nat. Electron.* **3**, 466–472 (2020).
60. Jin, X., Zhang, Y.-Y. & Du, S. Recent progress in the theoretical design of two-dimensional ferroelectric materials. *Fundam. Res.* **3**, 322–331 (2023).
61. Yu, J. et al. Photoinduced deterministic polarization switching in $CuInP_2$ S_6 for multifunctional optoelectronic logic gates. *Nano Lett*. acs.nanolett.4c05777. https://doi.org/10.1021/acs.nanolett.4c05777 (2025).
62. Zhang, J. et al. Ultrafast polarization switching via laser-activated ionic migration in ferroelectric CuInP2S6. *Phys. Rev. B* **111**, 104111 (2025).
63. Guan, Z., Ni, S. & Hu, S. Tunable electronic and optical properties of monolayer and multilayer janus MoSSe as a photocatalyst for solar water splitting: a first-principles study. *J. Phys. Chem. C.* **122**, 6209–6216 (2018).
64. Yin, W.-J. et al. Recent advances in low-dimensional Janus materials: theoretical and simulation perspectives. *Mater. Adv.* **2**, 7543–7558 (2021).
65. Tong, L. et al. 2D materials–based homogeneous transistor-memory architecture for neuromorphic hardware. *Science* **373**, 1353–1358 (2021).
66. Schroeder, U., Park, M. H., Mikolajick, T. & Hwang, C. S. The fundamentals and applications of ferroelectric HfO2. *Nat. Rev. Mater.* **7**, 653–669 (2022).
67. Hsain, H. A. et al. Many routes to ferroelectric HfO2: a review of current deposition methods. *J. Vac. Sci. Technol. A* **40** (2022).
68. Xiang, H. et al. Enhancing memory window efficiency of ferroelectric transistor for neuromorphic computing via two-dimensional materials integration. *Adv. Funct. Mater.* **33**, 2304657 (2023).
69. Chien, Y. et al. A MoS_2 hafnium oxide based ferroelectric encoder for temporal-efficient spiking neural network. *Adv. Mater.* **35**, 2204949 (2023).
70. Wu, X., Gao, S., Xiao, L. & Wang, J. WSe_2 negative capacitance field-effect transistor for biosensing applications. *ACS Appl. Mater. Interfaces* **16**, 42597–42607 (2024).

71. Ning, H. et al. An in-memory computing architecture based on a duplex two-dimensional material structure for in situ machine learning. *Nat. Nanotechnol.* **18**, 493–500 (2023).
72. Vizner Stern, M. et al. Interfacial ferroelectricity by van der Waals sliding. *Science* **372**, 1462–1466 (2021).
73. Deb, S. et al. Cumulative polarization in conductive interfacial ferroelectrics. *Nature* **612**, 465–469 (2022).
74. McCreary, K. M. et al. Stacking-dependent optical properties in bilayer WSe $_2$. *Nanoscale* **14**, 147–156 (2022).
75. Yang, T. H. et al. Ferroelectric transistors based on shear-transformation-mediated rhombohedral-stacked molybdenum disulfide. *Nat. Electron.* **7**, 29–38 (2023).
76. Yasuda, K. et al. Ultrafast high-endurance memory based on sliding ferroelectrics. *Science* **385**, 53–56 (2024).
77. Yan, X. et al. Moiré synaptic transistor with room-temperature neuromorphic functionality. *Nature* **624**, 551–556 (2023).
78. Zheng, Z. et al. Electronic ratchet effect in a moiré system: signatures of excitonic ferroelectricity. Preprint at https://doi.org/10.48550/arXiv.2306.03922 (2023).
79. Ma, C. et al. Intelligent infrared sensing enabled by tunable moiré quantum geometry. *Nature* **604**, 266–272 (2022).
80. Zhai, Y. et al. Reconfigurable 2D-ferroelectric platform for neuromorphic computing. *Appl. Phys. Rev.* **10**, 11408 (2023).
81. *Memristors and Memristive Systems*. https://doi.org/10.1007/978-1-4614-9068-5 (Springer New York, 2014).
82. Strukov, D. B., Snider, G. S., Stewart, D. R. & Williams, R. S. The missing memristor found. *Nature* **453**, 80–83 (2008).
83. Shan, X. et al. Emerging multimodal memristors for biorealistic neuromorphic applications. *Mater. Futures* **3**, 12701 (2024).
84. Thakkar, P., Gosai, J., Gogoi, H. J. & Solanki, A. From fundamentals to frontiers: a review of memristor mechanisms, modeling and emerging applications. *J. Mater. Chem. C.* **12**, 1583–1608 (2024).
85. Zhao, T. et al. Bio-inspired photoelectric artificial synapse based on two-dimensional $Ti_3C_2T_x$ MXenes floating gate. *Adv. Funct. Mater.* **31**, 2106000 (2021).
86. Wang, Y. et al. MXene-ZnO memristor for multimodal in-sensor computing. *Adv. Funct. Mater.* **31**, 2100144 (2021).
87. Ahmed, T. et al. Optically stimulated artificial synapse based on layered black phosphorus. *Small* **15**, 1900966 (2019).
88. He, H. et al. Photonic potentiation and electric habituation in ultrathin memristive synapses based on monolayer MoS_2. *Small* **14**, 1800079 (2018).
89. Cheng, Y. et al. Vertical 0D-perovskite/2D-MoS_2 van der waals heterojunction phototransistor for emulating photoelectric-synergistically classical pavlovian conditioning and neural coding dynamics. *Small* **16**, 2005217 (2020).
90. Wang, W. et al. Artificial optoelectronic synapses based on TiN_x O_{2-x} /MoS_2 heterojunction for neuromorphic computing and visual system. *Adv. Funct. Mater.* **31**, 2101201 (2021).
91. Sahu, M. C., Sahoo, S., Mallik, S. K., Jena, A. K. & Sahoo, S. Multifunctional 2D MoS_2 optoelectronic artificial synapse with integrated arithmetic and reconfigurable logic operations for In-memory neuromorphic computing applications. *Adv. Mater. Technol.* **8**, 2201125 (2023).
92. Dodda, A., Trainor, N., Redwing, Joan, M. & Das, S. All-in-one, bio-inspired, and low-power crypto engines for near-sensor security based on two-dimensional memtransistors. *Nat. Commun.* **13**, 3587 (2022).
93. Li, G. et al. Photo-induced non-volatile VO2 phase transition for neuromorphic ultraviolet sensors. *Nat. Commun.* **13**, 1729 (2022).
94. Zha, J. et al. A 2D heterostructure-based multifunctional floating gate memory device for multimodal reservoir computing. *Adv. Mater.* **36**, 2308502 (2024).
95. Sun, L. et al. In-sensor reservoir computing for language learning via two-dimensional memristors. *Sci. Adv.* **7**, eabg1455 (2021).
96. Chen, J. et al. Optoelectronic graded neurons for bioinspired in-sensor motion perception. *Nat. Nanotechnol.* **18**, 882–888 (2023).
97. Waser, R., Dittmann, R., Staikov, G. & Szot, K. Redox-based resistive switching memories – nanoionic mechanisms, prospects, and challenges. *Adv. Mater.* **21**, 2632–2663 (2009).
98. Yang, J. J., Strukov, D. B. & Stewart, D. R. Memristive devices for computing. *Nat. Nanotechnol.* **8**, 13–24 (2013).
99. Song, M.-K. et al. Recent advances and future prospects for memristive materials, devices, and systems. *ACS Nano* **17**, 11994–12039 (2023).
100. Jang, H. et al. Flexible neuromorphic electronics for wearable near-sensor and In-sensor computing systems. *Adv. Mater.* **37**, 2416073 (2025).
101. Van De Burgt, Y., Melianas, A., Keene, S. T., Malliaras, G. & Salleo, A. Organic electronics for neuromorphic computing. *Nat. Electron.* **1**, 386–397 (2018).
102. Wilson, J. A., Di Salvo, F. J. & Mahajan, S. Charge-density waves and superlattices in the metallic layered transition metal dichalcogenides. *Adv. Phys.* **24**, 117–201 (1975).
103. Grüner, G. The dynamics of charge-density waves. *Rev. Mod. Phys.* **60**, 1129–1181 (1988).
104. Hirata, T. & Ohuchi, F. S. Temperature dependence of the Raman spectra of 1T-TaS2. *Solid State Commun.* **117**, 361–364 (2001).
105. Samnakay, R. et al. Zone-folded phonons and the commensurate −incommensurate charge-density-wave transition in 1T-TaSe2 thin films. *Nano Lett*. **15**, 2965–2973 (2015).
106. Xi, X. et al. Strongly enhanced charge-density-wave order in monolayer NbSe2. *Nat. Nanotechnol.* **10**, 765–769 (2015).
107. Sayers, C. J. et al. Correlation between crystal purity and the charge density wave in 1 T – VSe 2. *Phys. Rev. Mater.* **4**, 25002 (2020).
108. Hossain, M. et al. Recent advances in two-dimensional materials with charge density waves: synthesis, characterization and applications. *Crystals* **7**, 298 (2017).
109. Vaskivskyi, I. et al. Fast electronic resistance switching involving hidden charge density wave states. *Nat. Commun.* **7**, 11442 (2016).
110. Khitun, A., Liu, G. & Balandin, A. A. Two-dimensional oscillatory neural network based on room-temperature charge-density-wave devices. *IEEE Trans. Nanotechnol.* **16**, 860–867 (2017).
111. Mihailovic, D. et al. Ultrafast non-thermal and thermal switching in charge configuration memory devices based on 1T-TaS2. *Appl. Phys. Lett.* **119**, 13106 (2021).
112. Liu, H. et al. A tantalum disulfide charge-density-wave stochastic artificial neuron for emulating neural statistical properties. *Nano Lett.* **21**, 3465–3472 (2021).
113. Li, W. & Naik, G. V. Light-induced reorganization of charge density wave stacking in 1T-TaS2. *Appl. Phys. Lett.* **118**, 253104 (2021).
114. Behera, S. K., Ahalawat, M. & Ramamurthy, P. C. Reconstructed electronic structure in 2D vdW 1T-TaS_2 for quantum sensing and information science. Preprint at https://doi.org/10.48550/arXiv.2404.14932 (2024).
115. Huang, W. C.-W. et al. Ultrafast optical switching to a heterochiral charge-density wave state. Preprint at https://doi.org/10.48550/arXiv.2405.20872 (2024).
116. Tilak, N. et al. Proximity induced charge density wave in a graphene/1T-TaS2 heterostructure. *Nat. Commun.* **15**, 8056 (2024).
117. Brown, J. O., Guo, T., Pasqualetti, F. & Balandin, A. A. Charge-density-wave oscillator networks for solving combinatorial optimization problems. Preprint at https://doi.org/10.48550/arXiv.2503.06355 (2025).
118. Lv, B. Q. et al. Unconventional hysteretic transition in a charge density wave. *Phys. Rev. Lett.* **128**, 36401 (2022).
119. Wu, D. et al. Layered semiconductor EuTe 4 with charge density wave order in square tellurium sheets. *Phys. Rev. Mater.* **3**, 24002 (2019).
120. Zhang, Q. Q. et al. Thermal hysteretic behavior and negative magnetoresistance in the charge density wave material EuTe 4. *Phys. Rev. B* **107**, 115141 (2023).

121. Rathore, R. et al. Evolution of static charge density wave order, amplitude mode dynamics, and suppression of kohn anomalies at the hysteretic transition in EuTe 4. *Phys. Rev. B* **107**, 24101 (2023).
122. Liu, Q. et al. Room-temperature non-volatile optical manipulation of polar order in a charge density wave. *Nat. Commun.* **15**, 8937 (2024).
123. Verma, A. et al. Picosecond volume expansion drives a later-time insulator–metal transition in a nano-textured mott insulator. *Nat. Phys.* **20**, 807–814 (2024).
124. Venturini, R. et al. Electrically driven non-volatile resistance switching between charge density wave states at room temperature. Preprint at https://doi.org/10.48550/arXiv.2412.13094 (2024).
125. Duan, S. et al. Identification of metastable lattice distortion free charge density wave at photoinduced interface via TRARPES. *npj Quantum Mater.* **10**, 16 (2025).
126. de la Torre, A. et al. Dynamic phase transition into a mixed-CDW state in 1T-TaS$_2$ via a thermal quench. Preprint at https://doi.org/10.48550/arXiv.2407.07953 (2025).
127. Boix-Constant, C. et al. Out-of-plane transport of 1T-TaS_2 /graphene-based van der waals heterostructures. *ACS Nano* **15**, 11898–11907 (2021).
128. Taheri, M. et al. Electrical gating of the charge-density-wave phases in two-dimensional *h* -BN/1T-TaS_2 devices. *ACS Nano* **16**, 18968–18977 (2022).
129. Shi, J. et al. Chemical vapor deposition grown wafer-scale 2D tantalum diselenide with robust charge-density-wave order. *Adv. Mater.* **30**, 1804616 (2018).
130. Yanase, T. et al. Unidirectional growth of epitaxial tantalum disulfide triangle crystals grown on sapphire by chemical vapour deposition with a separate-flow system. *CrystEngComm* **26**, 341–348 (2024).
131. Huang, B. et al. Layer-dependent ferromagnetism in a van der Waals crystal down to the monolayer limit. *Nature* **546**, 270–273 (2017).
132. Du, R. et al. Two-dimensional multiferroic material of metallic p-doped SnSe. *Nat. Commun.* **13**, 6130 (2022).
133. Bonilla, M. et al. Strong room-temperature ferromagnetism in VSe2 monolayers on van der waals substrates. *Nat. Nanotech.* **13**, 289–293 (2018).
134. Zhang, G. et al. Above-room-temperature strong intrinsic ferromagnetism in 2D van der waals Fe3GaTe2 with large perpendicular magnetic anisotropy. *Nat. Commun.* **13**, 5067 (2022).
135. Shao, D.-F. & Tsymbal, E. Y. Antiferromagnetic tunnel junctions for spintronics. *npj Spintron.* **2**, 13 (2024).
136. Jungwirth, T., Marti, X., Wadley, P. & Wunderlich, J. Antiferromagnetic spintronics. *Nat. Nanotechnol.* **11**, 231–241 (2016).
137. Lee, J.-U. et al. Ising-type magnetic ordering in atomically thin $FePS_3$. *Nano Lett.* **16**, 7433–7438 (2016).
138. Wang, X. et al. Electrical and magnetic anisotropies in van der Waals multiferroic CuCrP2S6. *Nat. Commun.* **14**, 840 (2023).
139. Song, Q. et al. Evidence for a single-layer van der Waals multiferroic. *Nature* **602**, 601–605 (2022).
140. Sattar, S., Islam, M. F. & Canali, C. M. Monolayer Mn X. and Janus, X Mn Y (X, Y= S, Se, Te): a family of two-dimensional antiferromagnetic semiconductors. *Phys. Rev. B* **106**, 085410 (2022).
141. Moinuddin, M. G., Srinivasan, S. & Sharma, S. K. Probing ferrimagnetic semiconductor with enhanced negative magnetoresistance: 2D chromium sulfide. *Adv. Electron. Mater.* **7**, 2001116 (2021).
142. Girovsky, J. et al. Long-range ferrimagnetic order in a two-dimensional supramolecular kondo lattice. *Nat. Commun.* **8**, 15388 (2017).
143. Li, X. & Yang, J. Toward room-temperature magnetic semiconductors in two-dimensional ferrimagnetic organometallic lattices. *J. Phys. Chem. Lett.* **10**, 2439–2444 (2019).
144. Fender, S. S., Gonzalez, O. & Bediako, D. K. Altermagnetism: a chemical perspective. *J. Am. Chem. Soc.* **147**, 2257–2274 (2025).
145. Song, C. et al. Altermagnets as a new class of functional materials. *Nat. Rev. Mater.* https://doi.org/10.1038/s41578-025-00779-1 (2025).
146. Reichlova, H. et al. Observation of a spontaneous anomalous hall response in the Mn5Si3 d-wave altermagnet candidate. *Nat. Commun.* **15**, 4961 (2024).
147. Regmi, R.B., Bhandari, H. & Thapa, B. Altermagnetism in the layered intercalated transition metal dichalcogenide CoNb4Se8. *Nat Commun* **16**, 4399 (2025).
148. Lawrence, E. A. et al. Fe site order and magnetic properties of $Fe_{1/4}NbS_2$. *Inorg. Chem.* **62**, 18179–18188 (2023).
149. Fert, A., Reyren, N. & Cros, V. Magnetic skyrmions: advances in physics and potential applications. *Nat. Rev. Mater.* **2**, 17031 (2017).
150. Bera, S. & Mandal, S. S. Theory of the skyrmion, meron, antiskyrmion, and antimeron in chiral magnets. *Phys. Rev. Res.* **1**, 033109 (2019).
151. Tey, M. S. N., Chen, X., Soumyanarayanan, A. & Ho, P. Chiral spin textures for next-generation memory and unconventional computing. *ACS Appl. Electron. Mater.* **4**, 5088–5097 (2022).
152. Crépieux, A. & Lacroix, C. Dzyaloshinsky–moriya interactions induced by symmetry breaking at a surface. *J. Magn. Magn. Mater.* **182**, 341–349 (1998).
153. Yu, X. Z. et al. Near room-temperature formation of a skyrmion crystal in thin-films of the helimagnet FeGe. *Nat. Mater.* **10**, 106–109 (2011).
154. Behera, A. K., Chowdhury, S. & Das, S. R. Magnetic skyrmions in atomic thin CrI3 monolayer. *Appl. Phys. Lett.* **114**, 232402 (2019).
155. Zhang, Y. et al. Generation of magnetic skyrmions in two-dimensional magnets via interfacial proximity. *Phys. Rev. B* **107**, 24402 (2023).
156. Hallal, A. et al. Rashba-type dzyaloshinskii–moriya interaction, perpendicular magnetic anisotropy, and skyrmion states at 2D materials/Co interfaces. *Nano Lett.* **21**, 7138–7144 (2021).
157. Sun, W. et al. Manipulation of magnetic skyrmion in a 2D van der Waals heterostructure via both electric and magnetic fields. *Adv. Funct. Mater.* **31**, 2104452 (2021).
158. Cui, Q. et al. Anisotropic Dzyaloshinskii–Moriya interaction and topological magnetism in two-dimensional magnets protected by $P\bar{4}m2$ crystal symmetry. *Nano Lett.* **22**, 2334–2341 (2022).
159. Bennett, D., Chaudhary, G., Slager, R.-J., Bousquet, E. & Ghosez, P. Polar meron-antimeron networks in strained and twisted bilayers. *Nat. Commun.* **14**, 1629 (2023).
160. Xia, J., Zhang, X., Liu, X., Zhou, Y. & Ezawa, M. Qubits based on merons in magnetic nanodisks. *Commun. Mater.* **3**, 88 (2022).
161. Huang, Y., Kang, W., Zhang, X., Zhou, Y. & Zhao, W. Magnetic skyrmion-based synaptic devices. *Nanotechnology* **28**, 08LT02 (2017).
162. Ahn, E. C. 2D materials for spintronic devices. *npj 2D Mater. Appl* **4**, 17 (2020).
163. Ikeda, S. et al. Magnetic tunnel junctions for spintronic memories and beyond. *IEEE Trans. Electron Devices* **54**, 991–1002 (2007).
164. Kumar, M. et al. Progress in multiferroic and magnetoelectric materials: applications, opportunities and challenges. *J. Mater. Sci. Mater. Electron.* **31**, 19487–19510 (2020).
165. Tabrizchi, S. et al. Magnetic-based integrated sensing and In/near-sensor processing:a comprehensive survey and future outlook. Preprint at https://doi.org/10.21203/rs.3.rs-4909455/v1 (2024).
166. Yang, H. et al. Two-dimensional materials prospects for non-volatile spintronic memories. *Nature* **606**, 663–673 (2022).
167. Kaverzin, A. A., Ghiasi, T. S., Dismukes, A. H., Roy, X. & van Wees, B. J. Towards fully two-dimensional spintronic devices. *2D Mater.* **9**, 045003 (2022).
168. Piquemal-Banci, M. et al. 2D-MTJs: introducing 2D materials in magnetic tunnel junctions. *J. Phys. D Appl. Phys.* **50**, 203002 (2017).

169. Wang, Z. et al. Tunneling spin valves based on Fe_3GeTe_2 /hBN/Fe_3GeTe_2 van der waals heterostructures. *Nano Lett.* **18**, 4303–4308 (2018).
170. Camsari, K. Y., Sutton, B. M. & Datta, S. p-bits for probabilistic spin logic. *Appl. Phys. Rev.* **6**, 11305 (2019).
171. Daniel, J. et al. Experimental demonstration of an on-chip p-bit core based on stochastic magnetic tunnel junctions and 2D MoS2 transistors. *Nat. Commun.* **15**, 4098 (2024).
172. Löhndorf, M. et al. Highly sensitive strain sensors based on magnetic tunneling junctions. *Appl. Phys. Lett.* **81**, 313–315 (2002).
173. Ota, S., Ando, A. & Chiba, D. A flexible giant magnetoresistive device for sensing strain direction. *Nat. Electron.* **1**, 124–129 (2018).
174. Liang, S. et al. Small-voltage multiferroic control of two-dimensional magnetic insulators. *Nat. Electron.* **6**, 199–205 (2023).
175. Behera, B., Sutar, B. C. & Pradhan, N. R. Recent progress on 2D ferroelectric and multiferroic materials, challenges, and opportunity. *Emergent Mater.* **4**, 847–863 (2021).
176. Guo, Y. et al. 2D multiferroicity with ferroelectric switching induced spin-constrained photoelectricity. *ACS Nano* **16**, 11174–11181 (2022).
177. Krempaský, J. et al. Efficient magnetic switching in a correlated spin glass. *Nat. Commun.* **14**, 6127 (2023).
178. Shao, D.-F., Zhang, S.-H., Li, M., Eom, C.-B. & Tsymbal, E. Y. Spin-neutral currents for spintronics. *Nat. Commun.* **12**, 7061 (2021).
179. Dong, J. et al. Tunneling magnetoresistance in noncollinear antiferromagnetic tunnel junctions. *Phys. Rev. Lett.* **128**, 197201 (2022).
180. Qin, P. et al. Room-temperature magnetoresistance in an all-antiferromagnetic tunnel junction. *Nature* **613**, 485–489 (2023).
181. Zhang, X. et al. Skyrmion-skyrmion and skyrmion-edge repulsions in skyrmion-based racetrack memory. *Sci. Rep.* **5**, 7643 (2015).
182. Koraltan, S. et al. Skyrmionic device for three dimensional magnetic field sensing enabled by spin-orbit torques. Preprint at https://doi.org/10.48550/arXiv.2403.16725 (2024).
183. Yokouchi, T. et al. Pattern recognition with neuromorphic computing using magnetic field–induced dynamics of skyrmions. *Sci. Adv.* **8**, eabq5652 (2022).
184. Gong, C. et al. Discovery of intrinsic ferromagnetism in two-dimensional van der waals crystals. *Nature* **546**, 265–269 (2017).
185. Ansari, M. S., Othman, M. H. D., Ansari, M. O., Ansari, S. & Abdullah, H. Progress in Fe3O4-centered spintronic systems: development, architecture, and features. *Appl. Mater. Today* **25**, 101181 (2021).
186. Plummer, D. Z. et al. 2D Spintronics for neuromorphic computing with scalability and energy efficiency. *J. Low Power Electron. Appl.* **15**, 16 (2025).
187. Wang, H. et al. Above room-temperature ferromagnetism in wafer-scale two-dimensional van der waals Fe_3GeTe_2 tailored by a topological insulator. *ACS Nano* **14**, 10045–10053 (2020).
188. Dankert, A., Venkata Kamalakar, M., Wajid, A., Patel, R. S. & Dash, S. P. Tunnel magnetoresistance with atomically thin two-dimensional hexagonal boron nitride barriers. *Nano Res* **8**, 1357–1364 (2015).
189. Dieny, B. et al. Opportunities and challenges for spintronics in the microelectronics industry. *Nat. Electron.* **3**, 446–459 (2020).
190. Kumari, S., Pradhan, D. K., Pradhan, N. R. & Rack, P. D. Recent developments on 2D magnetic materials: challenges and opportunities. *Emergent Mater.* **4**, 827–846 (2021).
191. Hao, Q. et al. 2D magnetic heterostructures and emergent spintronic devices. *Adv. Elect. Mater.* **8**, 2200164 (2022).
192. Leitao, D. C. et al. Enhanced performance and functionality in spintronic sensors. *Npj Spintron.* **2**, 54 (2024).
193. Zhao, Z., Lin, Y. & Avsar, A. Novel spintronic effects in two-dimensional van der Waals heterostructures. *npj 2D Mater. Appl.* **9**, 30 (2025).
194. Cui, Z. et al. Magnetic-ferroelectric synergic control of multilevel conducting states in van der waals multiferroic tunnel junctions towards in-memory computing. *Nanoscale* **16**, 1331–1344 (2024).
195. Piquemal-Banci, M. et al. Magnetic tunnel junctions with monolayer hexagonal boron nitride tunnel barriers. *Appl. Phys. Lett.* **108**, 102404 (2016).
196. Jayachandran, D. et al. Three-dimensional integration of two-dimensional field-effect transistors. *Nature* **625**, 276–281 (2024).
197. Schram, T. et al. WS2 transistors on 300 mm wafers with BEOL compatibility. In *Proc. 47th European Solid-state Device Research Conference (essderc)* 212–215. https://doi.org/10.1109/ESSDERC.2017.8066629 (IEEE, Leuven, Belgium, 2017).
198. Kim, K. S. et al. Non-epitaxial single-crystal 2D material growth by geometric confinement. *Nature* **614**, 88–94 (2023).
199. Zhou, Z. et al. Stack growth of wafer-scale van der Waals superconductor heterostructures. *Nature* **621**, 499–505 (2023).
200. Schranghamer, T. F., Sharma, M., Singh, R. & Das, S. Review and comparison of layer transfer methods for two-dimensional materials for emerging applications. *Chem. Soc. Rev.* **50**, 11032–11054 (2021).
201. Nakatani, M. et al. Ready-to-transfer two-dimensional materials using tunable adhesive force tapes. *Nat. Electron.* **7**, 119–130 (2024).
202. Kim, H. et al. High-throughput manufacturing of epitaxial membranes from a single wafer by 2D materials-based layer transfer process. *Nat. Nanotechnol.* **18**, 464–470 (2023).
203. Liu, Y., Huang, Y. & Duan, X. Van der Waals integration before and beyond two-dimensional materials. *Nature* **567**, 323–333 (2019).
204. Aubin, C. A. et al. Towards enduring autonomous robots via embodied energy. *Nature* **602**, 393–402 (2022).
205. Rodgers, M. M., Pai, V. M. & Conroy, R. S. Recent advances in wearable sensors for health monitoring. *IEEE Sens. J.* **15**, 3119–3126 (2015).
206. Wang, T.-Y. et al. Reconfigurable optoelectronic memristor for in-sensor computing applications. *Nano Energy* **89**, 106291 (2021).
207. Feng, G. et al. Flexible vertical photogating transistor network with an ultrashort channel for In-sensor visual nociceptor. *Adv. Funct. Mater.* **31**, 2104327 (2021).
208. Ji, R. et al. Fully light-modulated organic artificial synapse with the assistance of ferroelectric polarization. *Adv. Electron. Mater.* **8**, 2101402 (2022).
209. Haldane, F. D. M. Nobel lecture: topological quantum matter. *Rev. Mod. Phys.* **89**, 40502 (2017).
210. Kou, X., Fan, Y., Lang, M., Upadhyaya, P. & Wang, K. L. Magnetic topological insulators and quantum anomalous hall effect. *Solid State Commun.* **215–216**, 34–53 (2015).
211. Liu, Y. et al. Cryogenic in-memory computing using magnetic topological insulators. *Nat. Mater*. https://doi.org/10.1038/s41563-024-02088-4 (2025).
212. Zhu, T., Wang, H., Zhang, H. & Xing, D. Tunable dynamical magnetoelectric effect in antiferromagnetic topological insulator MnBi2Te4 films. *npj Comput. Mater.* **7**, 121 (2021).
213. Weber, B. et al. 2024 roadmap on 2D topological insulators. *J. Phys. Mater.* **7**, 22501 (2024).
214. Cucchi, I. et al. Microfocus laser–angle-resolved photoemission on encapsulated mono-, Bi-, and few-layer 1T′-WTe_2. *Nano Lett.* **19**, 554–560 (2019).
215. Xu, N., Xu, Y. & Zhu, J. Topological insulators for thermoelectrics. *npj Quantum Mater.* **2**, 51 (2017).
216. Wen, W., Dang, C. & Xie, L. Photoinduced phase transitions in two-dimensional charge-density-wave 1T-TaS_2 *. *Chin. Phys. B* **28**, 58504 (2019).
217. Freitas, P. P., Ferreira, R. & Cardoso, S. Spintronic sensors. *Proc. IEEE* **104**, 1894–1918 (2016).

Acknowledgements

This research was supported by National Science Foundation (NSF ECCS award no. 2441746) in addition to the Center for Semiconductor Manufacturing at the University of Arizona.

Author contributions

J.C., W.W., X.Y. wrote the manuscript and discussed the results at all stages. J.C. prepared all the figures. X.Y. supervised all aspects of the manuscript. All authors have read and approved the manuscript.

Competing interests

The authors declare no competing interests.

Additional information

Correspondence and requests for materials should be addressed to Xiaodong Yan.

Reprints and permissions information is available at http://www.nature.com/reprints

Publisher's note Springer Nature remains neutral with regard to jurisdictional claims in published maps and institutional affiliations.